TOPICAL REVIEW

Time-resolved two-photon photoemission from metal surfaces

Martin Weinelt

Lehrstuhl für Festkörperphysik, Universität Erlangen-Nürnberg, Staudtstr. 7, 91058 Erlangen, Germany

E-mail: weinelt@fkp.physik.uni-erlangen.de

Abstract

The Rydberg-like series of image-potential states is a prototype system for loosely bound electrons at a metal surface. The electronic structure and the femtosecond dynamics of these states is studied by high-resolution energy- and time-resolved two-photon photoemission spectroscopy. The electron trapped in the image potential moves virtually freely laterally to the surface where it is subject to inelastic and quasielastic scattering processes which cause decay of population and phase relaxation. The influence of surface corrugation on these processes has been investigated for adsorbates on Cu(001) and stepped Cu(117) and Cu(119) surfaces which are vicinal to Cu(001). The dynamics depend on both the distance of the electron in front of the surface and the parallel momentum. For CO molecules on Cu(001) inelastic scattering into bulk states and adsorbate-induced resonances determine the decay rate. For small numbers of Cu adatoms on Cu(001) and the vicinal surfaces the decay rate of image-potential states is significantly modified by interband and subsequent intraband scattering. On the vicinal surfaces the origin of the interband-scattering process is clarified as quasielastic scattering caused by disorder of the lateral superlattice. It occurs for electrons with group velocity perpendicular to the step edge and, moreover, exhibits a sizeable asymmetry. Electrons are mainly scattered into states with momentum in the upstairs direction. This asymmetry in quasielastic scattering explains the direction dependence of the lifetime of the first image-potential states on stepped Cu(119).

Contents

1. Introduction

Photoexcited electrons are of vital importance for a variety of processes at surfaces and interfaces [1]. Two-photon photoemission (2PPE) spectroscopy permits us to study the dynamics of excited electrons directly in the time domain [2, 3]. Besides understanding fundamental aspects [3–7] the driving power for this rather new research field is the impact of excited, hot electrons in chemical reactions [8] as well as the importance of electron transport through interfaces and surface recombination in semiconductor devices [2].

A number of review articles considering this topic have been published in recent years [2, 3, 9–11]. Semiconductor surfaces were among the first studied with time-resolved photoemission spectroscopy [2]. For low electron densities the dynamics at the surface is, as in the bulk, governed by electron–phonon scattering. Typical timescales are thus picoseconds. In addition dynamics is strongly influenced by surface defects giving rise to deep impurity levels [2, 12]. Hot-electron dynamics in noble metals is driven by inelastic electron–electron scattering [3, 13–15]. Decay and decoherence of excited bulk states happens in a few femtoseconds [3, 15]. Studies of magnetic surfaces of d metals allow us to elucidate spin-dependent dynamics [13, 16]. Hot electrons finally cause desorption of adsorbates [17–20] and if created by ultrashort laser pulses lead to new pathways in photochemical reactions [8].

Electron dynamics at surfaces encloses electron scattering in surface states [4, 11, 21–23]. Since in the majority of cases the latter are weakly coupled to the bulk continuum, decay and dephasing are slowed down [9, 10, 24]. This allows us to access fundamental aspects of inelastic and quasielastic electron scattering at surfaces [6, 7, 10, 25, 26]. Furthermore, for two-dimensional states photoemission is conceptually simple.

In the present article I will discuss a particular class of unoccupied surface states, so-called image-potential states. They can be viewed as loosely bound electrons in front of a metal surface [21, 27, 28]. Somewhat more precisely, an electron is trapped at a distance of a few ångstroms away from the surface by the image charge induced in the substrate, but can move virtually freely parallel to the surface. At first glance image-potential states just seem to be a curiosity [29]. However, their two-dimensional character allows us to study the dynamics of nearly free electrons as a function of parallel momentum and, even more promising, on a

shapeable template, i.e. the surface. Adsorbate layers and in particular noble gases are proven to change the coupling of image-potential states to bulk bands significantly and thereby influence electron dynamics [5, 7, 30–33]. In this work I concentrate on lateral modifications of the surface potential, such as small coverages of adatoms and molecules or regular arrangements of steps and adatoms. For the cases presented, there is no need to describe the electrons as being laterally localized. This implies that the electron in front of the surface averages over a sufficiently large surface area and inhomogeneous broadening is small. Electron dynamics is thus well described within the framework of optical Bloch equations [34]. Within this model time- and energy-resolved spectroscopy allows us to extract both inelastic and quasielastic scattering rates and thus to fully access electron dynamics.

The paper is organized as follows. Section 3 summarizes the main features of image-potential states on clean Cu(001) and Cu(111) surfaces. Following surfaces with negligible corrugation, the modifications due to a superlattice are discussed for Cu(117) and Cu(119) surfaces, which are vicinal to Cu(001) (section 4). For these surfaces angle-resolved measurements allow us to investigate the dynamics of electrons moving either upstairs or downstairs [35]. This reveals an asymmetry in quasielastic and inelastic scattering and enables us to clarify the nature of the interband-scattering process observed for clean Cu(001) [36] and to motivate the momentum dependence of lifetimes on Cu(119) [35]. While steps on vicinal surfaces are still rather regular, adsorption of a few Cu atoms or CO molecules on Cu(001) is used to create uncorrelated scattering centres. With increasing adsorbate coverage surface order is regained and the correlation between order and electron scattering is revealed (section 5) [7]. In the final section 6 dephasing and decay rates are compared for all systems studied. The concluding remarks highlight the main results and attempt an outlook on what can be done in the future. First, I will review the basics of femtosecond photoelectron spectroscopy and discuss the observables in 2PPE.

2. Energy- and time-resolved two-photon photoemission

A schematic energy diagram of the 2PPE process is shown in figure 1(a). A first laser pulse $3h\nu$ excites an electron from an initial state $|i\rangle$ below the Fermi level E_F into an unoccupied intermediate state $|n\rangle$. A second pulse $h\nu$ lifts the electron to the final state $|f\rangle$ above the vacuum level E_{vac}. Throughout this review $h\nu$ corresponds to infrared pulses from a Ti:sapphire oscillator and the ultraviolet pulse $3h\nu$ is obtained by frequency tripling a fraction of the infrared light (see section 2.4). Unless stated otherwise the photon energy referred to is the fundamental. Figure 1(a) illustrates two modes of data acquisition and corresponding spectra.

 (i) Energy-resolved 2PPE spectra are recorded at a particular delay between pump and probe pulses.
(ii) Electrons are registered for fixed kinetic energy as a function of time delay between pump and probe pulses.

This mode is also called time-resolved 2PPE. The information on dynamics of the electron in the intermediate state which can be extracted from either mode is discussed in the following sections. Beforehand, I illustrate a few spectroscopic basics of 2PPE (see also [21, 22, 28]).

2.1. Spectroscopy

2PPE is a second-order process, i.e. the signal follows the product of pump- and probe-pulse intensities. Direct photoemission would totally mask the 2PPE spectrum and has to be avoided. This prerequisite narrows the energy range of accessible unoccupied states between E_F and
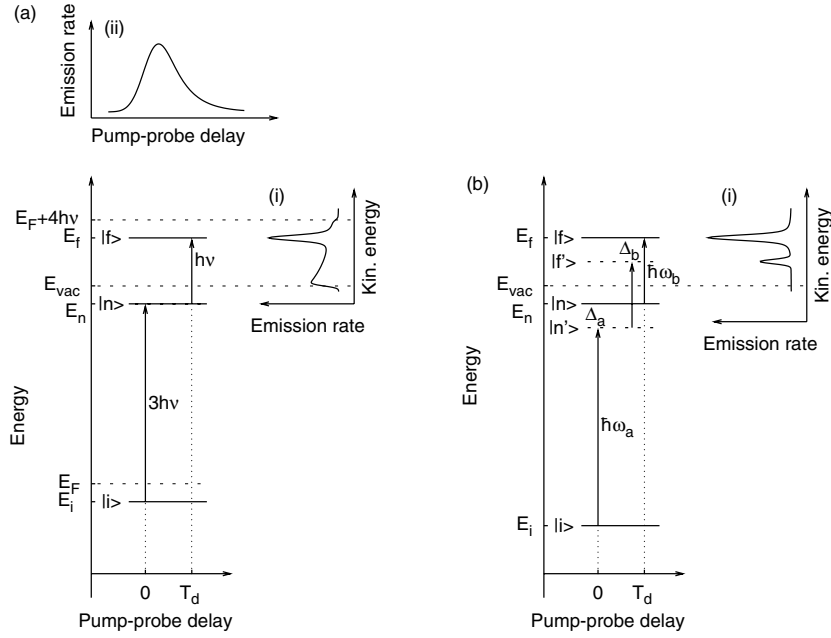
Figure 1. (a) Schematic representation of bichromatic 2PPE. The electron is excited from the occupied initial state $|i\rangle$ to the intermediate state $|n\rangle$ and final state $|f\rangle$ by the pump ($3h\nu$) and probe ($h\nu$) laser pulses. (i) Electrons are detected as a function of kinetic energy for fixed delay T_d between pump and probe pulses or (ii) for a fixed kinetic energy as a function of the time delay between pump and probe pulses. (b) General model for calculating 2PPE spectra including finite detunings Δ_a and Δ_b in the excitation and ionization steps.

E_{vac}. For a continuum of initial states the choice of the photon energy is usually straightforward, because there is always an initial state $|i\rangle$ below E_F to excite electrons to the intermediate state $|n\rangle$ and to the final state continuum $|f\rangle$. In all measurements presented photon energies of the laser pulses do not significantly exceed the sample work function Φ in order to suppress direct photoemission. However, the accessible momentum space (equation (1)) is limited by the rather small kinetic energies of the photoemitted electrons ($E_{kin} \leqslant 3h\nu \approx 4.65$ eV). Bichromatic 2PPE, i.e. using pulses with different photon energies, further restricts this energy range but allows us to discriminate between pump and probe processes. This is illustrated in figure 2(a) for Pd(111) [37]. The two transitions observed in the energy-resolved spectrum involve the Shockley surface state ($n = 0$) close to the bottom of the bandgap and the $n = 1$ image-potential state close to E_{vac} [38]. Both surface states are pumped from bulk states below E_F (dark-shaded area). While the image-potential state is excited by ultraviolet and probed by infrared light the reverse order is true for the Shockley surface state.

In the experiment, kinetic energies are measured with respect to the vacuum level of the analyser. The latter is linked to the Fermi level common to sample and analyser via the fixed analyser work function Φ_A. With appropriate bias voltage U the work function of the sample $\Phi > \Phi_A - eU$ is then obtained from the low-energy cut-off which is the zero of the kinetic-energy scale with respect to the sample.

The spectra in figure 2 have been recorded for normal emission. As is well known, the component of $\vec{k}$ parallel to the surface

$$k_{\parallel} = \sqrt{2mE_{kin}}/\hbar \sin \vartheta = 0.511\sqrt{E_{kin} \text{ (eV)}} \sin \vartheta \text{ (Å}^{-1}) \tag{1}$$
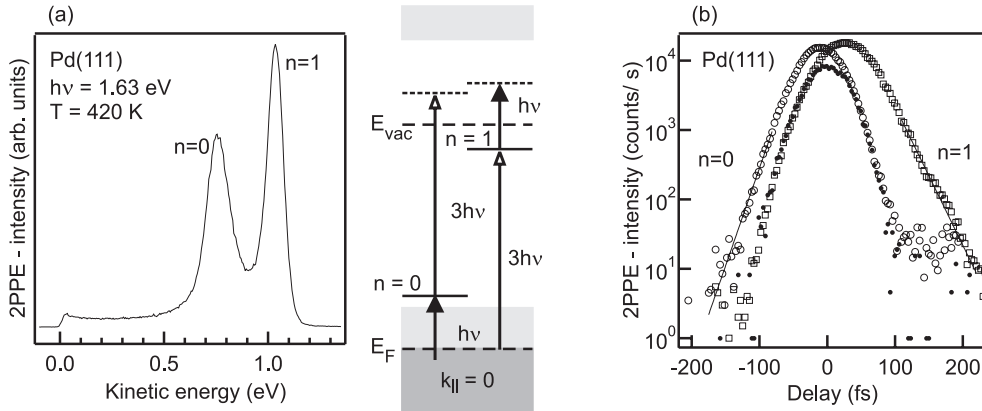
Figure 2. (a) Energy-resolved 2PPE spectrum for Pd(111) at $h\nu = 1.63$ eV. Intensity is plotted as a function of kinetic energy with respect to the Pd(111) sample [37]. Right panel: excitation scheme for Pd(111). The Shockley surface state ($n = 0$) is populated by a photon of energy $h\nu$. The image-potential state ($n = 1$) is excited by a photon with energy $3h\nu$. In the second step photon energies are interchanged. Surface-projected bulk bands along the surface normal are indicated by shaded areas. (b) Time-resolved measurements reveal the order of pump and probe processes and allow us to assign the observed transitions involving the Shockley surface state and the image-potential state. The solid dots show the cross-correlation of pump and probe pulses determined for the occupied Shockley surface state on Cu(111) at $h\nu = 1.63$ eV [37].

is conserved in photoemission. Since surface states are two dimensional by nature the intermediate state is completely determined by the kinetic energy E_{kin}, the emission angle ϑ (measured with respect to the surface normal) and the excitation sequence. For Pd(111) we thus probed the centre of the surface Brillouin zone (SBZ), i.e. $k_\parallel = 0$.

The above example illustrates that if surface states or surface resonances contribute to the 2PPE signal either as initial or intermediate states, the respective transitions in general dominate the 2PPE spectrum at the low photon energies used. This holds for most metals [21] and is in particular true for the 2PPE spectrum of Pd(111) in figure 2(a), which is evidently dominated by surface states. The flat and weak intensity-tail at kinetic energies below 0.5 eV is attributed to 2PPE involving bulk states above E_F. These unoccupied states are indicated by the lightly shaded areas in the left panel. In addition to 2PPE, intensity at low kinetic energies originates from one-photon photoemission of thermally excited electrons above E_F [21]. For the present example this contribution is, however, minor since the work function of Pd(111) ($\Phi = 5.50$ eV) is significantly larger than the chosen photon energy ($3h\nu = 4.89$ eV).

For Pd(111) the measurement was performed for overlapping pump and probe pulses. To illustrate how energy-resolved spectra depend on pump–probe delay typical room-temperature measurements for Cu(001) are shown in figure 3. The spectra exhibit three distinct peaks corresponding to emission from the $n = 1$, 2 and 3 image-potential states. These unoccupied states are energetically close to the vacuum level and therefore populated by the ultraviolet pulse and ionized by infrared light, i.e. the scheme shown in figure 1(a). As the time-delay increases, the intensity of the $n = 1$ state decays first. When the probe pulse is delayed by about 160 fs relative to the pump pulse, the intensity of the $n = 2$ state dominates the spectrum, showing that the latter state lives longer than the $n = 1$ state. At even larger delay only the signal of the $n = 3$ state and its shoulder arising from $n \geqslant 4$ states persists [39]. This observation qualitatively agrees with the theoretical prediction that the lifetime of image-potential states increases as n^3 [27]. Much more surprising is the fact that not only the intensity
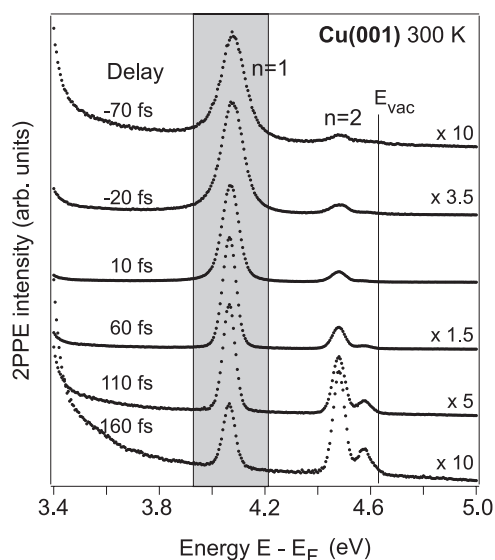
Figure 3. Energy-resolved 2PPE spectra for Cu(001) at 300 K for different delays between pump and probe pulses. The numbers on the right indicate the multiplication factors of the intensity data (see also [39]).

but also the linewidth depends on pump–probe delay. It is largest for negative delay, i.e. for a situation where the probe pulse arrives before the pump pulse and the 2PPE intensity can only arise due to the overlapping tails of both pulses. With increasing delay the linewidth decreases monotonically as most evident for the $n = 1$ image-potential state (grey-shaded area). Unfortunately, there is no simple explanation for this effect and I have to postpone a detailed analysis to section 2.3.2 until we have developed a rigorous description of the 2PPE process. Here we just note that there is no simple relation between linewidth and lifetime of the excited, intermediate state.

As already mentioned to determine the lifetime we have to perform time-resolved 2PPE. An example of such a measurement is shown in figure 2(b) for Pd(111). Here the analyser is tuned to the energy of the peak maxima in figure 2(a) and the relative pump–probe delay is scanned while recording the count rate of the photoelectrons. The curve shown by the solid dots is the cross-correlation trace of pump and probe pulses (see section 2.3.1). The maximum defines the optimum overlap between the laser pulses and thus delay zero. In the semi-logarithmic presentation of figure 2(b) the curve for the image-potential state ($n = 1$) shows a linear decay for positive delays which corresponds to $h\nu$ light arriving after the $3h\nu$ light at the sample. At negative delay the signal just follows the cross-correlation trace. In other words the image-potential state is pumped by ultraviolet and probed by infrared light. The reverse excitation order is true for the Shockley surface state. Thus the time-resolved measurements confirm the peak assignment given above. Alternatively, for surface states the pump–probe sequence can be determined by the photon-energy dependence of the kinetic energy [21, 38].

So far I have illustrated how a 2PPE experiment combines the state selectivity of conventional photoemission with the time resolution of pump–probe laser experiments. Lasers provide, however, not only short intense but also coherent light pulses. This implies that depending on the excitation scheme initial-, intermediate-and/or final-state wavefunctions

couple, e.g., to a state

$$|\Psi\rangle = \sum_{k \in \{i,n,f\}} c_k(t)|k\rangle, \qquad c_k(t) = |c_k(t)|e^{i\varphi_k(t)}e^{i\omega_k t}. \tag{2}$$

The temporal evolution of the excited state $|\Psi\rangle$ will thus not only involve population decay ($\propto |c_k|^2$) but also quantum phase relaxation, i.e. modifications of the initially well defined phase relation $\exp(i\varphi_k - i\varphi_l)$ between states $|k\rangle$ and $|l\rangle$ [3, 6, 40]. Inelastic scattering processes cause population decay. In contrast, all scattering processes which leave the population unchanged but alter the phase relation induced by the laser field are denoted quasielastic. Obviously, inelastic processes always cause phase relaxation. In practice, the division into inelastic and quasielastic scattering is somewhat arbitrary, since it depends on the energy and momentum resolution of the experiment. A more precise definition is given below. In the following sections we will see how inelastic and quasielastic scattering contributions can be separated by time- and energy-resolved 2PPE. I first recapitulate the density matrix formalism [34] which allows us to intuitively incorporate the concept of decay and dephasing [41, 42]. This leads to analytic expressions for the observables in time- and energy-resolved 2PPE [43]. The application to image-potential states is illustrated in section 3.

2.2. Modelling two-photon photoemission

The 2PPE process may be described by a fourth-order perturbation expansion in the electric fields [44]. I follow here the more common approach which models 2PPE in the framework of optical Bloch equations by numerical calculations [43, 45–47]. Figure 1(b) shows again the three-level system but now for the general excitation scheme, i.e. with finite detunings

$$\begin{aligned} \Delta_a &= \hbar\omega_a - (E_n - E_i) \\ \Delta_b &= \hbar\omega_b - (E_f - E_n). \end{aligned} \tag{3}$$

For $\Delta_a \neq 0$ the excitation is called off resonant. The energy-resolved spectrum contains two peaks ($|f'\rangle$ and $|f\rangle$ in figure 1(b)) denoted as either initial-or intermediate-state peaks according to their origin. Note that the transition from $|n'\rangle$ to $|f\rangle$ exhibits the detuning $\Delta_b = \Delta_a$ and results thus in an off-resonant contribution of the initial state $|i\rangle$. Initial, intermediate and final states are coupled via the laser field of pump and probe pulses $\vec{\mathcal{E}}(t) = \text{Re}(\vec{\epsilon}_a \mathcal{E}_a(t - T_d)e^{i\omega_a(t-T_d)} + \vec{\epsilon}_b \mathcal{E}_b(t)e^{i\omega_b t})$. The laser field is described by the envelopes $\mathcal{E}_a(t)$ and $\mathcal{E}_b(t)$ and the carrier frequencies ω_a and ω_b. $\vec{\mathcal{E}}(t)$ is assumed to be weak. Hence, the population of state $|f\rangle$ can be interpreted as the measured 2PPE signal. The energy-resolved spectrum is obtained by tuning the energy E_f and the time-resolved mode is modelled by changing the delay T_d, respectively. The dynamics of the three-level system is described in the Liouville–von Neumann formalism [34] by

$$\dot{\rho}_{kl} = \frac{1}{i\hbar}[\hat{H}_0 + \hat{V}, \hat{\rho}]_{kl} - \Gamma_{kl}\rho_{kl} \tag{4}$$

with the density operator $\hat{\rho}$, the Hamiltonian for the unperturbed three-level system $\hat{H}_0$ with eigenstates $|i\rangle, |n\rangle, |f\rangle$ and with $\hat{V}$ describing the interaction with the electric field. I assume bichromatic 2PPE where the pump pulse mediates only transitions between $|i\rangle$ and $|n\rangle$ and the probe pulse between $|n\rangle$ and $|f\rangle$ and introduce the notation $p_a(t) := \vec{\epsilon}_a \mathcal{E}_a(t - T_d)\langle i|\vec{D}|n\rangle$ and $p_b(t) := \vec{\epsilon}_b \mathcal{E}_b(t)\langle n|\vec{D}|f\rangle$. $\vec{D}$ is the dipole operator and $\hat{V} = |i\rangle p_a\langle n| + |n\rangle p_b\langle f| + \text{h.c.}$

Within the above formalism the decay rate (Γ_k) as well as the dephasing rate (Γ_k^*) of state $|k\rangle$ are phenomenologically introduced by the damping matrix $\hat{\Gamma}$ [41, 42]

$$\hat{\Gamma} = \begin{pmatrix} 0 & \frac{\Gamma_n}{2} + \Gamma_n^* + \Gamma_i^* & \Gamma_i^* + \Gamma_f^* \\ \frac{\Gamma_n}{2} + \Gamma_n^* + \Gamma_i^* & \Gamma_n & \frac{\Gamma_n}{2} + \Gamma_n^* + \Gamma_f^* \\ \Gamma_i^* + \Gamma_f^* & \frac{\Gamma_n}{2} + \Gamma_n^* + \Gamma_f^* & 0 \end{pmatrix}. \tag{5}$$

This choice restricts decay and dephasing to be exponential. The intermediate state has a finite lifetime $\tau_n = \hbar / \Gamma_n$, while those of initial and final states are assumed to be infinite ($\Gamma_i, \Gamma_f = 0$). After application of the rotating wave approximation [34] we obtain the optical Bloch equations

$$\dot{\rho}_{ii} = +\text{Im}(p_a^* \rho_{in}^{(1)})$$

$$\dot{\rho}_{nn} = -\text{Im}(p_a^* \rho_{in}^{(1)}) + \text{Im}(p_b^* \rho_{nf}^{(2)}) - \Gamma_{nn} \rho_{nn}$$

$$\dot{\rho}_{ff} = -\text{Im}(p_b^* \rho_{nf}^{(2)})$$

$$\dot{\rho}_{in}^{(1)} = -\text{i}\Delta_a \rho_{in}^{(1)} - \frac{\text{i}}{2} p_b^* \rho_{if}^{(3)} + \frac{\text{i}}{2} p_a (\rho_{nn} - \rho_{ii}) - \Gamma_{in} \rho_{in}^{(1)} \qquad (6)$$

$$\dot{\rho}_{nf}^{(2)} = -\text{i}\Delta_b \rho_{nf}^{(2)} + \frac{\text{i}}{2} p_a^* \rho_{if}^{(3)} + \frac{\text{i}}{2} p_b (\rho_{ff} - \rho_{nn}) - \Gamma_{nf} \rho_{nf}^{(2)}$$

$$\dot{\rho}_{if}^{(3)} = -\text{i}(\Delta_a + \Delta_b) \rho_{if}^{(3)} + \frac{\text{i}}{2} p_a \rho_{nf}^{(2)} - \frac{\text{i}}{2} p_b \rho_{in}^{(1)} - \Gamma_{if} \rho_{if}^{(3)},$$

wherein $\hbar = 1$ and $\rho_{in}^{(1)} := \text{e}^{-\text{i}\omega_a t}\rho_{in}$, $\rho_{nf}^{(2)} := \text{e}^{-\text{i}\omega_b t}\rho_{nf}$, $\rho_{if}^{(3)} := \text{e}^{-\text{i}(\omega_a + \omega_b)t}\rho_{if}$. By this transformation the detunings Δ_a and Δ_b contain all energy dependence. The diagonal elements of the density operator are real and represent the occupation probability $\rho_{kk} \propto |c_k|^2$ of state $|k\rangle$. The complex off-diagonal elements $\rho_{kl} = \rho_{lk}^*$ contain the phase information $\propto \exp(\text{i}\varphi_k - \text{i}\varphi_l)$ and describe the field-induced coupling of $|k\rangle$ and $|l\rangle$. When the pump pulse is over ($\mathcal{E}_a = 0$) and the probe pulse intensity is negligible ($\mathcal{E}_b \approx 0$) population ρ_{nn} and coupling ρ_{nf} decay freely $\rho_{nn} \propto \exp(-\text{i}\Gamma_n t)$ and $\rho_{nf} \propto \exp(-\text{i}(\Gamma_n/2 + \Gamma_n^* + \Gamma_f^*)t)$. As mentioned inelastic decay always causes dephasing and Γ_n enters both expressions. For distinction $\Gamma_{kl}^* = \Gamma_k^* + \Gamma_l^*$ is sometimes denoted as the pure dephasing rate.

The set of differential equations (6) allows us to simulate time- and energy-resolved 2PPE spectra by numerical calculation of $\rho_{ff}(T_d, \Delta_b)$ (see section 3.2.2). Analytic solutions for the steady state ($\mathcal{E}_{a,b} = \text{constant}$) have been discussed by Chebotayev [48] and later on refined for the case of 2PPE by Wolf *et al* [45]. This approach is, however, not applicable for 2PPE with femtosecond laser pulses since pulse duration and typical lifetime of the intermediate state are comparable. Here I focus on the limit of separated Gaussian pump and probe pulses where analytic expressions have been derived. An extended analysis is given in [43].

2.3. Population decay and phase relaxation

An ultrashort laser pulse with a bandwidth of 50 meV suitable for photoelectron spectroscopy exhibits a duration of $\approx$40 fs. For a compilation of the time–bandwidth products $\Delta t \Delta \omega$ for common pulse shapes see table 1. As mentioned the lifetime of unoccupied surface states ranges from a few femtoseconds up to several hundred picoseconds. This suggests that in most cases the lifetime and linewidth of surface states can be determined when the pump process is over.

2.3.1. Lifetime measurements Consider again the time-resolved spectra in figure 2(b). Data are depicted on a semi-logarithmic scale after background subtraction. The cross-correlation trace (solid dots) has a full width at half maximum (FWHM) of 58 fs and defines the time span where pump and probe pulses overlap, i.e. $\mathcal{E}_a(t - T_d)\mathcal{E}_b(t) \neq 0$. For sufficient delay the pump process no longer influences the population of the intermediate state and the signal decays exponentially. The lifetime is extracted from the linear slope in the semi-logarithmic plot [39] and exact knowledge of delay zero is dispensable. This way we obtain $\tau_0 = 13 \pm 3$ fs and $\tau_1 = 25 \pm 5$ fs for the Shockley surface state ($n = 0$) and the $n = 1$ image-potential state

Table 1. Pulse shapes $p(t)$ of laser pulses. When the pulse duration T_p (FWHM) is given in femtoseconds the bandwidth (FWHM) is obtained in units of meV by $658\Delta\omega_b$. The linewidth Γ of the intermediate-state peak in 2PPE is calculated for separated pump and probe pulses and in the limit of large probe-pulse duration. Hyperbolic secant (sech) and exponential pulses have the same asymptotic behaviour.

Pulse shape	Function $p(t)/p_0$	Duration $T_p B$	Bandwidth $\Delta\omega_b$	Linewidth
Gauss	$e^{-(Bt)^2}$	$\sqrt{2\ln 2}$	$2.773/T_p$	$2\Gamma_n^* + 2\Gamma_f^*$
Sech	$2/(e^{Bt} + e^{-Bt})$	$2\ln(\sqrt{2}+1)$	$1.979/T_p$	$\Gamma_n + 2\Gamma_n^* + 2\Gamma_f^*$
Exponential	$e^{-B|t|}$	$\ln 2$	$0.892/T_p$	$\Gamma_n + 2\Gamma_n^* + 2\Gamma_f^*$
Cosine	$\cos^2(Bt), |Bt| < \pi/2$	$2\arccos\sqrt[4]{1/2}$	$3.299/T_p$	$\sim 0.6\Gamma_n + 1.5(\Gamma_n^* + \Gamma_f^*)$

on Pd(111). The values are in excellent agreement with theoretical calculations [37]. Note that beside short pulses an essential ingredient to evaluate the decay rate from the exponential tail of the signal is the high sensitivity required to obtain data with a dynamic range of at least three orders of magnitude [39].

As seen by the Shockley surface state for lifetimes of about 10 fs the above evaluation is at the limit. For even broader cross-correlation, lower count rates or shorter lifetimes one is drawn back to determine the decay rate by equations (6). As input parameter we need pump- and probe-pulse durations. It turns out that the evaluation depends critically on the accurate knowledge of the zero on the timescale rather than the exact pulse shapes. The latter can, e.g., be assumed to be Gaussian. Delay zero is fixed by the maximum of the cross-correlation trace, which therefore has to be determined at the sample position. This is usually done by off-resonant excitation of either initial or intermediate surface states. From equations (6) it follows that large detuning Δ leads to strong oscillations of the off-diagonal elements $\dot{\rho}_{kl} \propto -i\Delta\rho_{kl}$. Thus the population ρ_{nn} follows the envelope of the excitation pulse ($p_a \propto \mathcal{E}_a(t)$) and the 2PPE signal $\rho_{f'f'}$ yields the cross-correlation $\propto \int dt\, \mathcal{E}_a(t - T_d)\mathcal{E}_b(t)$ [42]. For the measurements on Pd(111) depicted in figure 2(b) the response of the occupied Shockley surface state on Cu(111) was used as reference. Since this approach is common practice I have to add some words of caution. As on the Pd(111) surface, we find on Cu(111) an unoccupied image-potential state which serves as intermediate state $|n\rangle$ with finite lifetime and dephasing rate [3, 25, 39]. For excitation at $h\nu = 1.63$ eV, the photon energy where data on Pd(111) have been recorded, the detuning corresponds to $\Delta_a = 400$ meV and delay zero is well defined by the maximum of the cross-correlation curve. Already at a detuning of 180 meV ($h\nu = 1.55$ eV) off-resonant contributions $|n\rangle \to |f'\rangle$ increase significantly and the maximum of the initial-state peak in the time-resolved measurement is shifted to finite delay time $T_d = 3.7$ fs, i.e., no longer reflects delay zero. Cross-correlation traces are routinely recorded before and after each time-resolved spectrum and allow us to check for eventual drifts. With time zero at hand, evaluation of the time-resolved Pd(111) spectra by equations (6) yields lifetimes of 11.5 ± 3 fs for the Shockley state and 22 ± 5 fs for the image-potential state in good agreement with the direct evaluation from the exponential tail (see figure 4).

Wolf and co-workers pointed out that for short lifetimes and sufficiently short pulses (FWHM of cross-correlation $\leqslant 100$ fs) already the shift between the maximum of the cross-correlation trace and the maximum of the signal of the probed intermediate state corresponds within typical error bars ($\sim \pm 3$ fs) to the lifetime [49]. To give a limit, this is certainly correct for lifetimes below 25 fs whenever large dephasing in the pump process $\Gamma_{12}^* \geqslant 100$ meV occurs. This is in general fulfilled when bulk states serve as initial states. A typical timescale for dephasing of bulk states is $\leqslant 5$ fs [3, 50–55]. For rapid dephasing (large Γ^*) we reach the limit of rate equations where the population increase follows the pulse envelope. Hence the
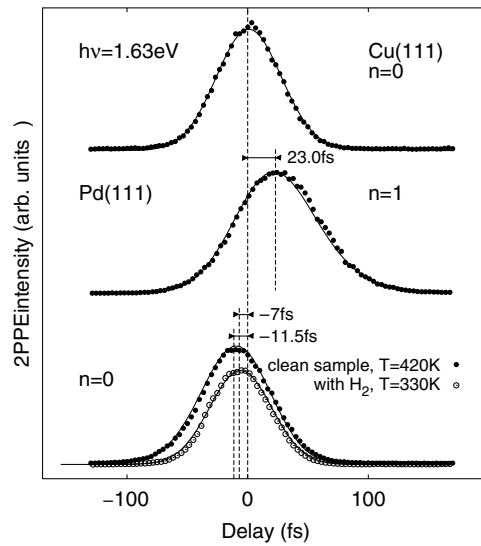
Figure 4. Time-resolved measurements of figure 2(b) (solid circles). Lines correspond to fits solving equations (6). The shift of the peak maxima with respect to the maximum of the cross-correlation is a good approximation for the lifetime. Data recorded after 30 min at a sample temperature of 330 K (open circles) show the sensitivity of the Shockley surface state to surface contamination by H_2 adsorption from the residual gas (base pressure 2×10^{-11} mbar).

maximum is fairly well described by the convolution of the pump pulse and an exponential ($\propto e^{-\Gamma t}$). As this is also the case for Pd(111), the shifts indicated in figure 4 yield the correct lifetimes within ± 2 fs.

Whatever method is used to evaluate the lifetime of a surface state already early photoemission work demonstrated that decay rates, extracted via $\tau = \hbar / \Gamma$ from linewidth analysis, depend sensitively on surface order [56]. From the shift between spectra in figure 4 bottom (open and solid circles) we see that the lifetime of the Shockley surface state on Pd(111) decreases by about a factor of two upon hydrogen adsorption. This is the reason why data presented in figure 2 have been measured at 420 K, where H_2 adsorption is avoided. It is well known that Cu surfaces are by far less sensitive to adsorption of rest gas and therefore suitable as a reference. However, surface defects, such as (frizzy) steps or adatoms, will be always present and will modify decay rates. In this sense measurements of the lifetime probe surface quality and thereby surface preparation and, not surprisingly, the error range of lifetimes is usually larger than expected from spectroscopic restraints.

2.3.2. Linewidth analysis. In conventional photoemission it is common practice to extract the photo-hole lifetime τ by linewidth analysis assuming a Lorentzian lineshape with an FWHM of $\Gamma = \hbar / \tau$. To extract this inelastic decay rate requires all other contributions to the linewidth to be known or negligible. This includes in particular quasielastic scattering processes, such as electron–phonon or defect scattering, and has been done by extrapolation to zero temperature [57] or zero defect density [58–60]. As discussed above in 2PPE the decay rate Γ_n of the unoccupied intermediate state is accessible by time-resolved measurements. As long as inhomogeneous broadening can be neglected, the linewidth analysis should thus allow us to determine the dephasing rates Γ_k^*. Since we are primarily interested in the dynamics of the intermediate state, i.e. the values of Γ_n and Γ_n^*, we ignore the pump process ($\mathcal{E}_a = 0 = p_a$)

and assume that the population of the intermediate state decays with some effective decay rate $\rho_{nn} = \rho_{nn}^0 e^{-\Gamma' t}$. The probe pulse $\mathcal{E}_b$ is centred at $t = 0$ and the population of the intermediate state pumped at time $t = -T_d$ decreased according to $\rho_{nn}^0 \propto e^{-\Gamma' T_d}$.

If we, furthermore, assume a weak probe pulse $\mathrm{Im}(p_b^* \rho_{nf}^{(2)}) \ll \Gamma' \rho_{nn}$, the population of the intermediate state is not significantly influenced, i.e. $\rho_{ff} \ll \rho_{nn}$. This reduces the set of equations (6) to

$$\dot{\rho}_{nf}^{(2)} + (\mathrm{i}\Delta_b + \Gamma_{nf})\rho_{nf}^{(2)} = -\frac{\mathrm{i}}{2} p_b \rho_{nn}^0 e^{-\Gamma' t}$$
$$\dot{\rho}_{ff} = -\mathrm{Im}(p_b^* \rho_{nf}^{(2)})$$

(7)

and reads in integral form

$$\rho_{nf}^{(2)}(t) = -\frac{\mathrm{i}}{2} \int_{-\infty}^{\infty} \mathrm{d}t' \, e^{-(\mathrm{i}\Delta_b + \Gamma_{nf})(t-t')} \Theta(t - t') p_b(t') \rho_{nn}^0 e^{-\Gamma' t'}$$

(8)

$$\rho_{ff}(t) = -\mathrm{Im}\left\{ \int_{-\infty}^{t} \mathrm{d}t' \, p_b^*(t') \rho_{nf}^{(2)}(t') \right\}.$$

(9)

The 2PPE intensity $I := \rho_{ff}(t \to \infty)$ is given by the double integral in equation (9). Noticing that the integral $\int \mathrm{d}t' \, e^{(\mathrm{i}\Delta_b + \Gamma_{nf})t'} \ldots$ contains the Fourier transformation $\mathcal{F}$ with respect to the detuning Δ_b, one obtains after some algebra [43]

$$I = \frac{\rho_{nn}^0}{2} \mathrm{Re}\{\mathcal{F}(e^{-(\Gamma_n^* + \Gamma_f^* + \Gamma_n/2 - \Gamma'/2)\tau} \Theta(\tau)) * |\mathcal{F}(p_b(\tau)e^{-\frac{1}{2}\Gamma' \tau})|^2\}.$$

(10)

The intensity I depends on T_d via $\rho_{nn}^0 \propto e^{-\Gamma' T_d}$. Since the pump process was assumed to be over, information on dephasing of the initial state is not contained in the linewidth at large delay T_d. Obviously, for separated pump and probe pulses it is of no importance whether the intermediate state is resonantly populated ($\Delta_a = 0$) or not. The linewidth at large delay contains two contributions.

(i) The first term in equation (10) describes a Lorentzian peak with the width $2\Gamma_n^* + 2\Gamma_f^* + \Gamma_n - \Gamma'$. Let us assume that the effective decay rate of the intermediate state is mainly determined by the intrinsic inverse lifetime, i.e. $\Gamma_n \approx \Gamma'$. Since the final state is an evanescent state we can furthermore neglect dephasing $\Gamma_f^* \approx 0$. The width of the Lorentzian is thus only defined by the dephasing rate of the intermediate state Γ_n^*.

(ii) This Lorentzian is convoluted ($*$) with a function determined both by the electric field envelope of the probe pulse p_b and the decay rate of the intermediate state Γ'. Through the latter coupling, the probe-pulse envelope ($p_b(t) \propto \mathcal{E}_b(t)$) influences the measured linewidth [43]. To illustrate this consider a Gaussian-shaped pulse. Since the product of an Gaussian and an exponential is just a shifted Gaussian, the Fourier transfom $\mathcal{F}$ does not depend on the decay rate Γ' of the intermediate state, but only on the bandwidth $\Delta\omega_b$ of the probe laser pulse. In consequence for a Gaussian-shaped probe pulse the Lorentzian contribution to the intermediate-state peak (FWHM) at large pump–probe delay is nothing but the dephasing rate $2(\Gamma_n^* + \Gamma_f^*) \approx 2\Gamma_n^*$.

Results for commonly assumed probe-pulse shapes are summarized in table 1. For hyperbolic secant pulses (sech in table 1) the linewidth depends on the pulse duration in a very intricate way [43]. Here only the result for large probe-pulse duration is given. Obviously, it is mandatory to characterize the probe pulse in order to extract the dephasing rate from a linewidth measurement even for separated pump and probe pulses.

Probably, for the reader used to conventional photoemission spectroscopy and $\Gamma_n = \hbar/\tau_n$ the dependence of the linewidth on the exact shape of the probe pulse, i.e. the tails, is surprising.

The subtle difference between the two photoemission techniques is that in conventional photoemission the initial state population is constant and the photo-hole decay starts with the excitation process, while in the 2PPE experiment an increasing or decreasing electron population is probed at time delay T_d.

2.3.3.   Time-resolved coherent spectroscopy   In principle time-resolved coherent spectroscopy contains more information since it probes the phase relation between the wavefunctions of the states coupled by the laser field. Compared to pure optical techniques 2PPE is state selective but the applicability of coherent spectroscopy techniques is unfortunately limited [3, 6, 7, 61]. There are two 2PPE techniques to measure the pure dephasing rates with rather high precision directly in the time domain.

(i) A two-pulse interferometric photoemission experiment is much like a typical autocorrelation measurement. Two pulses with identical polarization and frequency ω are collinearly overlapped on the sample and the photoelectrons are recorded as a function of pump–probe delay. Dephasing shows up in the ω and 2ω components of the correlation trace [3]. While the ω signal contains as well the information on the decay rate of the intermediate state as the coupling to the intermediate state Γ^*_{in} and Γ^*_{nf} the 2ω component yields Γ^*_{if} [3]. The technique has been mainly applied to determine dephasing and decay rates of hot electrons and their implications on photochemical reactions [19]. For sufficient statistics in 2PPE such interferometric measurements require in general extreme stability of the whole experimental setup and rather short pulses [3]. Experiments have been so far realized on metal surfaces with visible light pulses ($2h\nu \sim 3.1$ eV) only. This photon energy restricts accessible initial and intermediate states on clean surfaces. To overcome the problem, the sample work function is often lowered by adsorption of alkalis [3, 13]. As already pointed out and discussed in detail in section 5.2, even small amounts of defects (adsorbates) can alter the dynamics of surface states tremendously. Thus while interferometric measurements are extremely powerful to determine dephasing rates directly in the time domain, the general applicability is restricted. For a critical review see also [62].

(ii) Quasielastic scattering rates can also be extracted by quantum beat spectroscopy. This method is only applicable for a few favourable systems to which, fortunately, the Rydberg-like series of image-potential states on metal surfaces belongs [6]. As described in section 3.1 the energy spacing of higher image-potential states is below the bandwidth of the exciting laser pulse. The coherent excitation of these energetically close but separated levels by the pump pulse leads to quantum interference between the excited states. In other words a wavepacket is formed by the superposition of several states with initially fixed phase relation [6]. This results in a quantum beat pattern (see figure 5) [6].

The process can be described by equation (4) introducing additional intermediate states [6]. A somewhat more intuitive approach is given in [7]. Consider again equation (2) for two intermediate states, e.g., n and $n + 1$. For sufficient delay the signal is described by the superposition

$$|c_n(t)|^2 + |c_{n+1}(t)|^2 + 2|c_n(t)||c_{n+1}(t)| \cos((\omega_n - \omega_{n+1})t). \tag{11}$$

The parameters $|c_n|^2$ and $|c_{n+1}|^2$ describe the intensities of states $|n\rangle$ and $|n + 1\rangle$ in the time-resolved 2PPE measurement. For two coherently excited states we observe oscillations on top of the time-resolved signal with a period $T = 2\pi/(\omega_n - \omega_{n+1}) = h/(E_n - E_{n+1})$ [6, 7].

In the absence of events which lead to pure dephasing (nearly realized for the clean Cu(001) surface), the well defined initial phase relation is retained and the damping of the interference
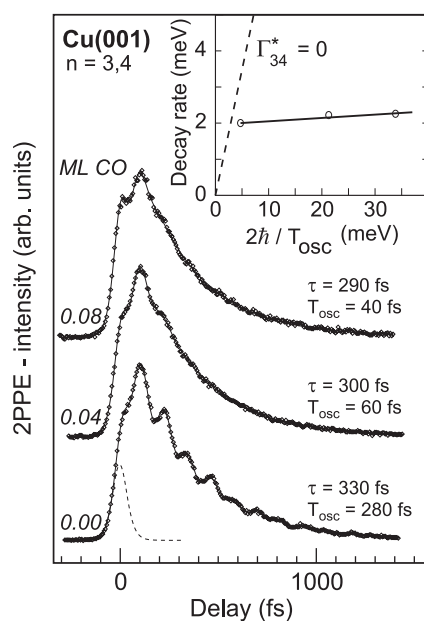
Figure 5. Time-resolved measurements for CO on Cu(001) (see also figure 2 in [7]). Coherent excitation of $n = 3$ and 4 image-potential states leads to quantum beats superimposed on the decay of the $n = 3$ population. The inset compares population decay and decay rate of the oscillations ($2\hbar/T_{osc}$). The dashed curve indicates the expected trend in the absence of pure dephasing.

pattern solely follows population decay. Quasielastic scattering events leave the electron in its excited state but destroy phase coherence. Consequently, the quantum interference is damped faster than the overall intensity [7, 63]. Thus quantum beat spectroscopy provides a direct means to study quasielastic and inelastic scattering processes of electrons at metal surfaces. This is illustrated in figure 5 where spectra for the Cu(001) sample with and without small amounts of CO are depicted. For the measurements the analyser was tuned to the energetic position of the $n = 3$ image-potential state and the signal recorded as a function of pump–probe time delay [7]. For the clean surface the coherent excitation of the $n = 3$ and 4 image-potential states leads to oscillations with a period of 117 fs superimposed on an exponential decay representing mainly the lifetime τ_3 of the $n = 3$ image-potential state [7]. Decay and dephasing rates have been evaluated as described in [7]. For the clean surface we find similar decay and dephasing times ($\tau = 330$ fs and $T_{osc} = 280$ fs). The situation changes, however, dramatically with CO adsorption. Even a small coverage of CO molecules (4% of a monolayer) is sufficient to effectively destroy the initial phase coherence, while the overall signal decays with a nearly unchanged time constant of $\tau = 300$ fs [7]. Oscillations are now only visible up to 200 fs and the dephasing time T_{osc} is reduced to a value of 60 fs. This trend is retained by doubling the CO coverage. In the inset of figure 5 decay rate $\hbar/\tau$ and dephasing rate $2\hbar/T_{osc}$ are compared. In the absence of pure dephasing contributions ($\Gamma_{34}^* = \Gamma_3^* + \Gamma_4^* = 0$) the data points would coincide with the dashed curve. The almost negligible slope of the straight line through data points demonstrates in contrast that the population decay rate changes only slightly, while the dephasing rate and thus the pure dephasing rate Γ_{34}^* increase significantly [10].

2.3.4. Observables in two-photon photoemission. The observables in 2PPE and their relation to decay and dephasing are schematically summarized in figure 6. Inelastic scattering leads to
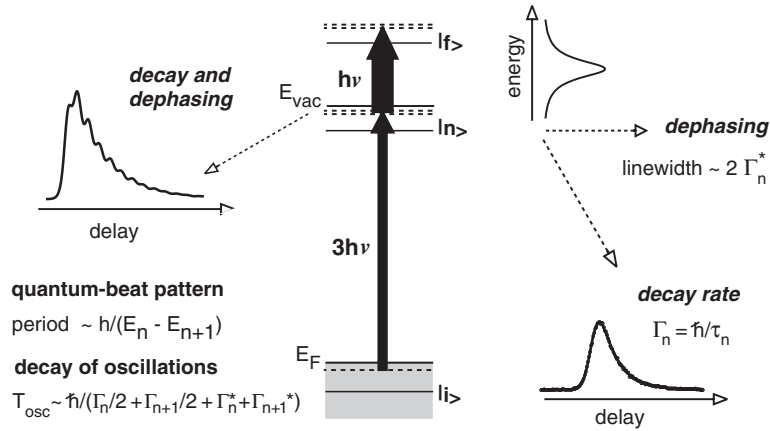
Figure 6. Schematics of the observables in 2PPE and their relation to decay and dephasing processes.

decay of the intermediate-state population with a rate $\hbar/\tau_n$. In contrast quasielastic scattering does not alter the population of the image-potential state but destroys phase coherence [10]. In principle the pure dephasing rate contains contributions from all states involved in the excitation process: the photo-hole in the initial state Γ_i^*, the intermediate states Γ_n^* and the evanescent final state Γ_f^*, respectively [45]. For sufficient delay between pump and probe pulses only intermediate and final states have to be considered. The problem is further reduced assuming that dephasing is negligible in the final state [45]. Phase-breaking events in the intermediate state result in a Lorentzian contribution $\mathcal{F}(e^{-\Gamma_n^* t})$ to the linewidth (right panel). The actual measured contribution depends, however, on the shape of the probe pulse $p_b \propto \mathcal{E}_b(t)$. Likewise, an extra damping of the evolving quantum beat pattern occurs due to dephasing of coherently excited states (left panel). If only two states are involved the oscillations are damped with a time constant of

$$T_{osc} = \hbar(\Gamma_n/2 + \Gamma_{n+1}/2 + \Gamma_n^* + \Gamma_{n+1}^*)^{-1} \tag{12}$$

whereas the overall signal decay is dominated by the population decay of the shorter-lived state [7].

2.4. Experimental approach

The experimental setup for 2PPE spectroscopy can be divided into two parts:

 (i) a laser system to generate femtosecond pump and probe pulses and
(ii) an ultrahigh-vacuum system equipped with a suitable photoelectron spectrometer.

The setup used in our laboratory is sketched in figure 7.

 (i) Photon energies around the sample work function are necessary to populate or probe unoccupied states close to E_{vac} or E_F, respectively. Ultraviolet light (UV, $3h\nu$) is generated by frequency tripling the output of a Ti:sapphire oscillator. The infrared fundamental (IR, $h\nu$) is sufficient for the other excitation step. For the investigation of different substrates or adsorbate layers tuning of the oscillator wavelength is desired. For spectroscopy it is mandatory.
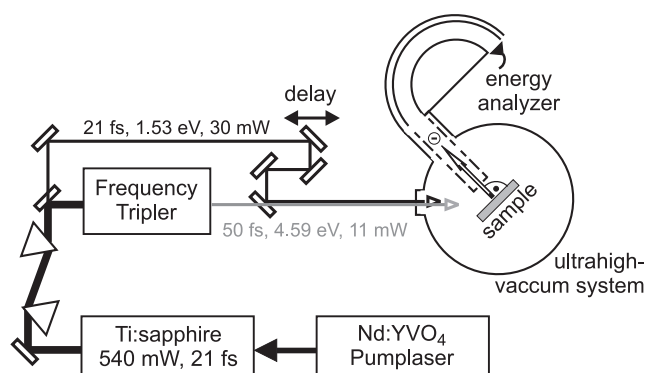
Figure 7. Experimental setup for time-resolved 2PPE.

The homebuilt Ti:sapphire oscillator generates IR pulses with a central wavelength of 790 nm ($h\nu = 1.57$ eV) and a duration of 21 fs at a repetition rate of 86 MHz. The average output power amounts to 540 mW. The pump laser is a diode-pumped solid-state laser (Millenia, Spectra Physics) running at 4.2 W. The design of the oscillator is similar to the one described in [64]. Prism pairs are used to compensate for second-order dispersion in the cavity and after the output coupler. Tuning of the oscillator wavelength between 750 and 820 nm is realized by introducing a slit in the output arm of the cavity.

The main part (90%) of the IR beam is used for frequency tripling ($3h\nu = 4.71$ eV at 790 nm). After second-harmonic generation (LBO, type I) the remaining IR pulse is compressed by a prism pair and mixed with the visible (BBO, type I). Final compression yields UV pulses of $\geqslant 45$ fs length with the average power ranging between 3 and 12 mW depending on the chosen wavelength.

To adjust the delay between pump and probe pulses the rest (10%) of the IR beam from the oscillator passes a computer-controlled delay stage and is combined with the UV light. For most time-resolved measurements a step width of 0.5 μm corresponding to a delay time of 3.35 fs was used. A delay stage and tripler are mounted on a breadboard in a compact setup avoiding long beam paths. Drifts between two subsequent time-resolved spectra are usually below 1 fs.

IR and UV pulses are finally focused collinearly onto the sample. Spot position on the sample is controlled via a magnified image on an IR-sensitive video camera. This allows us to readjust the beam rather precisely when the sample is rotated with respect to the surface normal or exchanged. The incidence angle α is either 45° or 80°. Pulse compression also accounts for the fused silica input windows. Polarization of beams is adjustable.

The IR pulses are characterized by interferometric autocorrelation and the wavelength spectrum [62, 65, 66]. The $3h\nu$ pulse duration is determined via the cross-correlation as described in section 2.3.1. While changing the fundamental wavelength is fairly simple, it requires tuning phase matching and prism compressors in the tripler as well as the delay between UV and IR pulses. To adjust the system to a new wavelength usually takes half an hour.

(ii) The ultrahigh-vacuum chamber comprises the components for sample preparation and characterization. A 125 mm hemispherical electron analyser equipped with five channeltrons (EA 125, Omicron) is used for electron detection. The energy resolution of the analyser, measured by the width of the low-energy cut-off, is typically set to 20 or 30 meV, which is achieved at pass energies of 1.5 or 2 eV, respectively. The kinetic energies

of the excited electrons are typically around 1 eV. Therefore, a specially designed lens-voltage table (low mag mode for ultraslow electrons, Omicron) and magnetic shielding as well as field compensation by Helmholtz coils are used to achieve proper transmission of the spectrometer. Spectra at normal emission are usually measured with a negative bias of 0.5–3 V on the sample. To study $k_\parallel$-dependent observables the bias is reduced to 0–0.5 eV. In this measurement mode transmission is reliable above 0.7 eV. The angular resolution was determined by the $k_\parallel$-dependence of the linewidth of the $n = 1$ image-potential state on Cu(001) to $\pm 1.5°$.

3. Image-potential states on clean metal surfaces

Image-potential states at metal surfaces were first predicted by Echenique and Pendry [27] and later on verified by inverse photoemission [67, 68]. 2PPE spectroscopy resolved the first three members of the Rydberg-like series [69, 70]. First time-resolved studies were performed by Schoenlein and co-workers [71–73]. Further progress arose with the introduction of Ti:sapphire-based laser systems [6, 74]. For reviews see [21, 22, 28, 75, 76].

3.1. Basic concept

Since the theory of image-potential states is well established [11, 21, 27, 77] we briefly recapitulate a few basic aspects exemplified by Cu(001) and Cu(111). The surface and the underlying bulk Brillouin zones are sketched in figure 8 together with the projected bulk band-structure along $\overline{\Gamma M}$. Both surface orientations exhibit surface-projected bandgaps centred at $\overline{\Gamma}$. Such sizeable gaps which support surface states occur indeed for all low-index noble-metal surfaces [78]. An electron in front of the surface is trapped in the potential well generated by the attractive image force and the bandgap. The surface plane is usually chosen to be at half a lattice spacing beyond the last atomic layer [79] and a one-dimensional model potential is used to calculate image-potential-state wavefunctions [21, 27, 77, 79–81]. As illustrated in figure 9 the coulombic tail of the image potential

$$V = E_{vac} - \frac{e^2}{4\pi\epsilon_0}\frac{1}{4z}, \qquad z > 0 \tag{13}$$

supports a Rydberg-like series of states, labelled by the quantum number n, with energies

$$E_n - E_{vac} = -\frac{m}{32}\left(\frac{e^2}{4\pi\epsilon_0\hbar}\right)^2\frac{1}{(n+a)^2} = -\frac{0.85\ \text{eV}}{(n+a)^2}, \qquad n = 1, 2, \ldots. \tag{14}$$

The binding energy E_n is corrected by the so-called quantum defect a which depends on the width of the bandgap and its position with respect to the reference level E_{vac} [27]. A scattering model, which accounts for phase shift of the wavefunction upon reflection at the surface barrier, yields $a = 0 - 0.5$ from top to bottom of the bandgap [77].

On Cu(111) the $n = 1$ image-potential state is close to the top of the bandgap where bulk states have s character. By matching the hydrogen-like solution in the image potential to the bulk solution the wavefunction vanishes at $z = 0$ and we obtain $a = 0$. As depicted in figure 9 the probability density of the $n = 1$ image-potential state has a node at the surface plane and the maximum is located ~ 2.3 Å away from the surface [82]. For Cu(001) the Rydberg-like series lies in the middle of the bandgap and the bulk penetration is reduced. In addition, the maximum of the probability density is shifted further outside the surface to 3.8 Å [82]. Consequently, the binding energy of the image-potential states is lowered [21] and E_1 is best described by $a = 0.20$. For higher image-potential states the mean distance of the electron shifts to larger distances z as $\approx n^2$ and the wavefunction penetrates less into the bulk (probability density $\approx n^{-3}$).
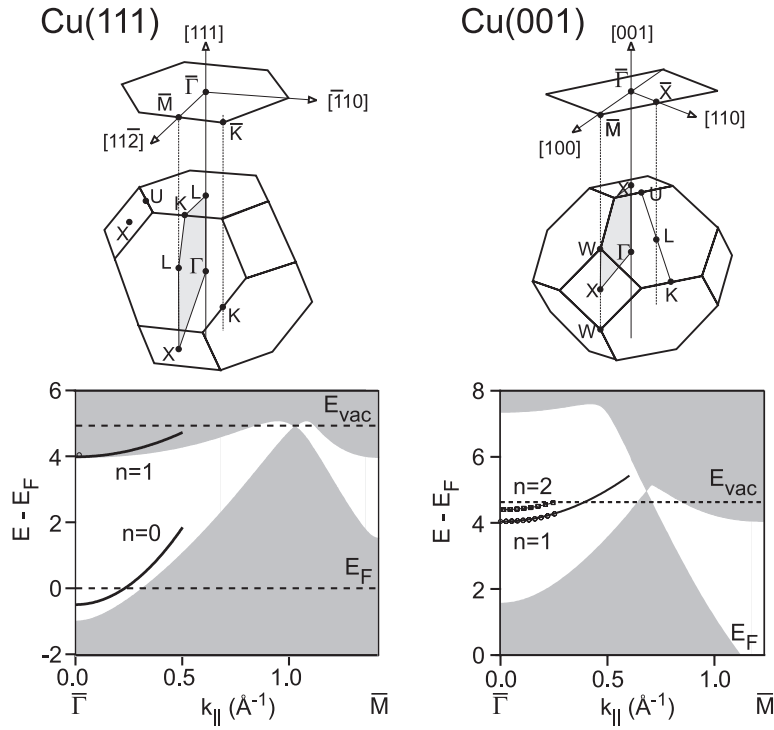
Figure 8. SBZ and surface-projected bulk band structure of Cu(111) (left panel) and Cu(001) (right panel). The sp gap of the projected bulk band structure (shaded areas) supports the Rydberg-like series of unoccupied image-potential states $n = 1, 2, \ldots$. The occupied Shockley surface state on Cu(111) is labelled $n = 0$.
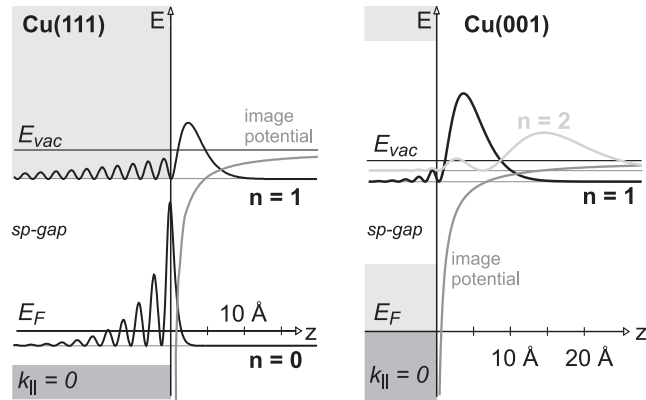

Figure 9. Left panel: bandgap for Cu(111) at $k_{\parallel} = 0$. The $1/4z$ image potential is indicated by the dark grey curve. The solid curves display the probability density and energetic position for the occupied Shockley surface state ($n = 0$) and the $n = 1$ image-potential state. $n \geqslant 2$ states are already degenerate with the bulk continuum. Right panel: bandgap for Cu(001) at $k_{\parallel} = 0$. Solid curves display the probability density for the $n = 1$ and 2 image-potential states. The centre of gravity shifts to larger z-values with increasing quantum number n.

Table 2. Binding energies E_n, effective masses m_n^*/m_0, lifetimes τ_n, decay rates $\Gamma_n = \hbar/\tau_n$ and dephasing rates Γ_n^* for image-potential states on Cu(001), Cu(111), Cu(119) and Cu(117). For Cu(111) see also [29]. Work functions Φ and quantum defects a_1 for $n = 1$ and $a_{\geqslant 2}$ for $n \geqslant 2$ image-potential states are listed. The error for energy values is ± 10 meV; the error for effective masses m_n^*/m_0 is ± 0.1.

n	E_n (meV)	m_n^*/m_0	τ_n (fs)	τ_n (fs)[a,b]	Γ_n (meV)	Γ_n^* (meV)
		Cu(001), $\Phi = 4.63$ eV, $a_1 = 0.20$, $a_{\geqslant 2} = 0.17$				
1	590	0.8	35 ± 6	30/38	19 ± 3	<5
2	180	0.9	120 ± 15	132/164	5.5 ± 0.7	<1
3	85	1.0	300 ± 20	367/480	2.2 ± 0.15	<1
4	50	—	630		1.045	<1
5	32	—	1200		0.55	<1
		Cu(111), $T = 300$ K ($T = 100$ K), $\Phi = 4.93$ eV, $a = 0$				
1	840 (810)	1.3	18 ± 5 (23 ± 5)	17	36.5 ± 10 (29 ± 6)	20 ± 10 (5 ± 5)
2	220	—	14 ± 3	—	47 ± 10	—
3	95	—	40 ± 6	—	16.5 ± 2.5	—
		Cu(119), $\Phi = 4.60$ eV, $a_1 = 0.24$, $a_{\geqslant 2} = 0.20$				
1	556	1.05	15 ± 5		44 ± 15	40 ± 5
2	176	1.15	39 ± 3		17 ± 1.5	<5
3	84	1.15	105 ± 15		7 ± 1	<2
4	48	—	200 ± 20		3.3 ± 0.4	<2
5	31	—	350 ± 40		1.9 ± 0.2	<2
		Cu(117), $\Phi = 4.59$ eV, $a_1 = 0.24$, $a_{\geqslant 2} = 0.17$				
1	550	1.0	15 ± 5		44 ± 15	40 ± 5
2	171	1.0	39 ± 5		17 ± 2	<5
3	83	1.05	95 ± 15		6.3 ± 1.1	<2
4	48	—	190 ± 20		3.5 ± 0.4	<2
5	31	—	350 ± 40		1.88 ± 0.2	<2

[a,b] Calculated values from (a) [24] and (b) [82].

From the above model description it is obvious that electrons excited to image-potential states can be viewed as being loosely bound in front of the metal surface. For most surfaces the effective mass is close to the free electron mass, i.e. motion parallel to the surface is nearly unhindered (see table 2). The somewhat larger effective mass of the $n = 1$ image-potential state on Cu(111) is attributed to band structure effects due to the energetic position of this state close to the upper band edge[1]. The decoupling from bulk states leads to enlarged lifetimes and allows us to access the dynamics of the electron in the intermediate state with femtosecond photo-electron spectroscopy. This includes both inelastic and quasielastic scattering processes which lead to decay of the intermediate-state population and quantum phase relaxation. In section 2.3 we have seen how these quantities can be extracted by energy- and time-resolved 2PPE spectroscopy. In the following these concepts are applied to the clean Cu(001) and Cu(111) surfaces.

3.2. Clean Cu(001) and Cu(111) surfaces

First experimental studies on the image-potential state were performed on Cu surfaces [67, 68]. Since then Cu(001) and Cu(111) have been investigated extensively (see [6, 10, 39, 69, 83–85] and [74, 84, 86]). In the present study the Rydberg-like series of image-potential states on

[1] The same value has been observed for $n = 1$ on Ag(111) with a comparable position of the image-potential state in the bandgap [87].
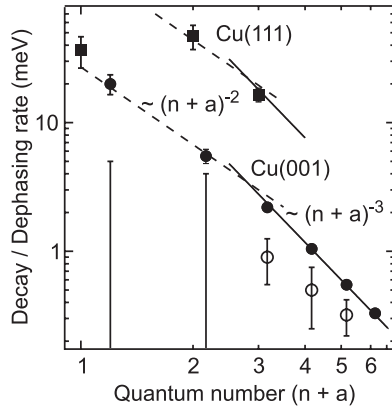
Figure 10. Decay rates for the image-potential states on Cu(001) (solid circles) and Cu(111) (solid squares) as a function of quantum number $n + a$. Open circles display the pure dephasing rates on Cu(001) (see also figure 7 in [10]).

Cu(001) serves as a well characterized and conceptually simple model system to investigate electron dynamics at related metal surfaces. To give an overview, energies, effective masses, decay and dephasing rates for Cu(001), Cu(111), Cu(119) and Cu(117) are summarized in table 2. Values are gathered from [6, 10, 24, 39] and this work.

3.2.1. Decay rates. We solely consider decay rates at the band bottom of the image-potential-state parabola and postpone a discussion on momentum dependence until section 4.4. According to many-body theory the major inelastic decay mechanism at metal surfaces is electron–hole pair excitation via screened Coulomb interaction [11]. A rough estimate for the decay rate of image-potential states may be obtained by weighting the respective decay rate of bulk electrons with the bulk penetration p_{bulk} [21, 27, 87, 88]. Since p_{bulk} scales as n^{-3} for large quantum number [27] we expect the decay rate to scale according to $\Gamma = p_{bulk}\Gamma_{bulk} \propto n^{-3}\Gamma_{bulk}$. The decay rate of unoccupied bulk states Γ_{bulk} is shown to increase linearly, i.e. moderately, with energy E for $E \geqslant E_n \approx E_F + 5$ eV [89–94]. Thus for higher-image-potential states ($n \geqslant 3$), with negligibly small energy separation the decay rate should simply scale $\propto n^{-3}$. This qualitative argument has already been put forward by Echenique and Pendry in their early theoretical study of image-potential states to ensure the integrity of the Rydberg series [27]. An alternative illustration of the n^{-3}-dependence of the decay rate is obtained by calculating the period of the oscillatory motion of a classical electron in the image potential [10]. Analogous to Kepler's law the round-trip time in a $1/z$-potential is $T^2 \propto d^3$. Since the mean distance d is $\propto n^2$, one obtains $T_n = 2.43(n+a)^3$ fs [10]. Inelastic scattering occurs predominantly at the surface. Consequently, the collision rate $1/T_n$ suggests a decay rate $\propto (n+a)^{-3}$. Moreover, within this simple model the variation of the decay rate with n should not depend on details of the electronic or geometric structure of the surface [10, 63].

Image-potential states up to $n = 6$ on Cu(001) were first resolved in the quantum beat experiments of Höfer *et al* [6]. In figure 10 the decay rates for Cu(001) (solid circles) are depicted as a function of quantum number $n + a$. As indicated by the solid straight line the estimate of the simple bulk penetration model $\Gamma_n \propto (n + a)^{-3}$ holds well for $n \geqslant 3$. For $n \leqslant 3$ a weaker dependence $\propto (n+a)^{-2}$ is observed (dashed line) [10, 39]. Calculated decay rates for $n \leqslant 3$ on Cu(001) are listed in table 2 [24, 82]. As pointed out in [11] decay rates for Cu(001) are estimated correctly within 30% by the bulk penetration. This is due to the
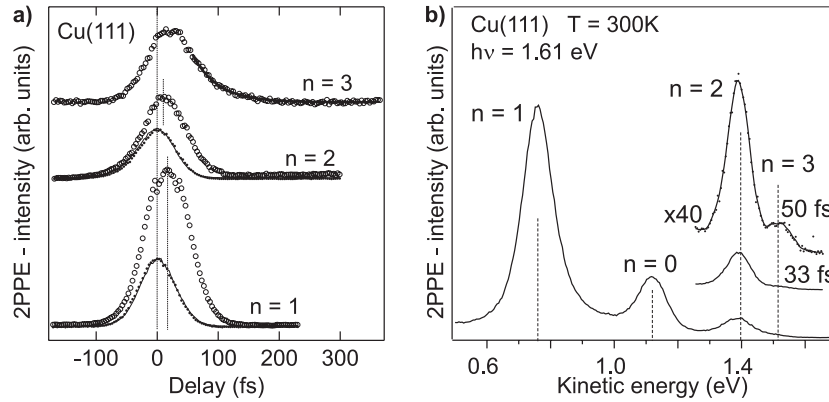
Figure 11. (a) Time-resolved measurements for the $n = 1, 2$ and 3 image-potential states on Cu(111) (open circles) measured at a photon energy of 1.61 eV. Solid circles and full curves show the cross-correlation determined for the occupied Shockley surface state ($n = 0$) before and after the respective time-resolved measurement. For $n = 1$ and 2 image-potential states the lifetime is evaluated from the shift with respect to the cross-correlation trace, while for $n = 3$ the exponential decay after the cross-correlation trace is used. (b) Energy-resolved spectra for Cu(111). At sufficient pump–probe delay (50 fs) the $n = 3$ image-potential state is resolved.

fact that contributions of interface and vacuum to the decay rate nearly cancel each other. Inelastic interband decay from $n \geqslant 2$ image-potential states to the respective lower bands ($|n + 1\rangle \rightarrow |n\rangle$) is calculated to give a contribution of ≈ 10–15% of the total decay rate for $n = 2$ and 3 states [82]. While the agreement of experiment and most advanced theory for the $n = 1$ state is quite satisfying, calculated decay rates for $n = 2$ and 3 are still too low [82].

For Cu(111) the situation is somewhat more intricate. Since the energetic position of the $n = 1$ image-potential state falls just below the upper edge of the bandgap at $\overline{\Gamma}$, states with $n \geqslant 2$ are degenerate with bulk states [74, 75, 86]. Thus the bulk penetration increases significantly for $n \geqslant 2$ and so does the decay rate. Time-resolved measurements for the first three image-potential states on Cu(111) are depicted in figure 11. Decay rates listed in table 2 are evaluated from the shift of the maxima with respect to the cross-correlation trace. As shown in figure 10 the decay rate increases from $n = 1$ to 2 but again parallels that for Cu(001) for $n = 2$ and 3 (the offset between straight lines in figure 10 is identical).

The sizeable bulk penetration p_{bulk} of the $n = 1$ state on Cu(111) (see figure 9) leads to a significant overestimate of the decay rate at 421 meV [21]. The bulk penetration p_{bulk} is, however, compensated by the lack of decay channels near $\overline{\Gamma}$ (see figure 8) and decay into unoccupied bulk states is predicted to yield a lifetime comparable to Cu(001) [95]. While Cu(001) has only a surface resonance, the Shockley surface state on Cu(111) contributes significantly to the decay rate of the image-potential states. Theory predicts that this additional decay channel makes 40% of the $n = 1$ inverse lifetime on Cu(111) [24, 95].

3.2.2. Dephasing rates. Since inelastic and quasielastic scattering (decay and pure dephasing) takes place at the surface one naively expects from the classical collision model the branching ratio of both processes to be independent of the quantum number n. As discussed in section 2.3.3 and [7] the concept of dephasing is most easily seen for higher-image-potential states on Cu(001). The time-resolved measurements in figure 12 reveal oscillations with a period of 117 and 230 fs corresponding to energy differences of coherently excited states $n = 3, 4$ and $4, 5$. While the overall signal decays with $\tau \approx \hbar / \Gamma_3$ the quantum interference
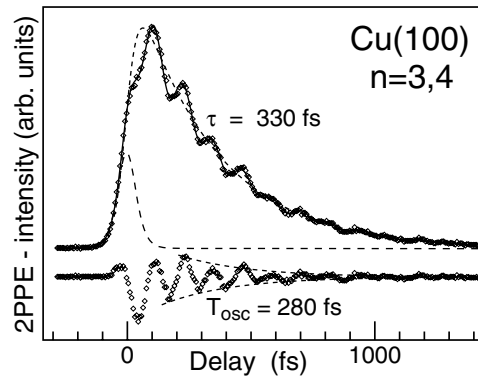
Figure 12. Time-resolved 2PPE measurement of Cu(001). The analyser energy is tuned to the energy of the $n = 3$ image-potential state. The average intensity and the quantum beats decay with the time constants τ and T_{osc}, respectively (dashed curves). The long-dashed curve shows the cross-correlation between probe and pump pulses and defines delay zero [10].
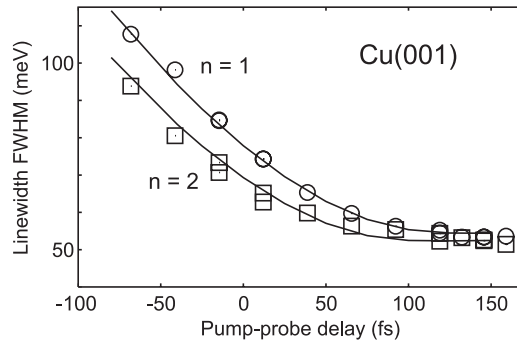

Figure 13. Measured (open symbols) and calculated (solid curves) linewidths of the $n = 1$ and 2 image-potential states on Cu(001) [43]. For the calculation Gaussian-shaped laser pulses were used. The experimental uncertainties are within the symbol size. Fit parameters and results are listed in table 3.

decays according to equation (12). This allows us to extract combined dephasing rates $\Gamma_n^* + \Gamma_{n+1}^*$. The individual dephasing rates for $n \geqslant 3$ depicted in figure 10 have been estimated assuming a $(n + a)^{-3}$ dependence of Γ_n^*.

Image-potential states $n = 1$ and 2 are not excited coherently since their energy separation is larger than the bandwidth of the laser pulses. However, with the decay rate determined, the pure dephasing rate Γ_n^* can be extracted from energy-resolved spectra at large pump–probe delay assuming Gaussian laser pulses (see section 2.3.2). A set of energy-resolved spectra for Cu(001) was depicted in figure 3. As already discussed, the linewidth decreases with increasing delay between pump and probe pulses. Since the signal to background ratio is excellent, data analysis is straightforward even for spectra recorded at large delay. Experimentally determined linewidths (FWHM) for $n = 1$ (open circles) and $n = 2$ (open squares) image-potential states are gathered in figure 13.

With the model developed in section 2.3.2 linewidths are evaluated by numerical calculations. The results are shown as solid lines in figure 13. For Cu(001) electrons are excited from a continuum of initial states giving rise to resonant and off-resonant contributions. As dephasing of initial bulk states is rapid, incoherent summation is appropriate. Spectra are

Table 3. Fit parameters of the linewidth analysis in figure 13. Decay rate Γ_n and pulse bandwidth $\Delta\omega$ are independently determined by time-resolved 2PPE. Gaussian shape of pump and probe pulses is assumed.

	Γ_1 (meV)[a]	Γ_2 (meV)	$\Delta\omega_{pump}$ (meV)	$\Delta\omega_{probe}$ (meV)	Γ_1^* (meV)	Γ_2^* (meV)
Fit	18.3	5.1	49	29	2.0	0.1
Exp.	18 ± 3	5.5 ± 1	53 ± 3	25 ± 4	< 54	< 5

[a] From [39] and this work.

therefore calculated for many discrete initial states and then added up assuming a free-electron density of states. The analyser resolution is accounted for by summation over final states weighted with a Gaussian analyser function, respectively. In spite of the different decay rates of the $n = 1$ and 2 states the linewidths for large pump–probe delay are almost identical. With increasing negative delay, i.e. both pulses still overlap but the maximum of the probe pulse arrives before the maximum of the pump pulse, the linewidth shows a linear increase which is independent of the lifetime. As shown analytically in [43] this is a signature for Gaussian-shaped excitation pulses. Hence for the numerical calculation (solid curves in figure 13) Gaussian laser pulses are assumed. Table 3 compares experimental data with the results from the simulation.

Widths of pump and probe pulses are estimated from autocorrelation and cross-correlation measurements, respectively. Overall fit parameters and experimental values are in good agreement and thus the obtained pure dephasing rates are reliable. As discussed in section 2.3.2 for a Gaussian probe pulse the dephasing rate Γ^* can be directly extracted from the linewidth at large pump–probe delay. Note that the Lorentzian contribution of the dephasing rate to the linewidth is $2\Gamma^*$. Taking the analyser resolution (20 meV) and experimental bandwidth of the probe pulse (53 meV) into account the contribution of Γ_1^* as well as Γ_2^* has to be small (<5 meV).

A different situation is found for Cu(111) where the linewidth of the $n = 1$ image-potential state depends noticeably on sample temperature [25]. This is attributed to electron–phonon coupling. Its importance for Cu(111), but not for Cu(001), can be understood noticing the different bulk penetration [25] (see figure 9). From a detailed investigation of the temperature dependence Knoesel, Hotzel and Wolf derived a mass-enhancement parameter $\lambda = 0.06$ for the $n = 1$ image-potential state [25] as compared to $\lambda = 0.14$ for the occupied Shockley state [25, 57, 96]. Data for Cu(111) have been analysed assuming sech pulses as previously described in [49]. While this affects the extracted absolute values of the dephasing rate, the influence on λ is negligible. The latter correlates nicely with the respective wavefunction overlap of the $n = 1$ and 0 states with the bulk continuum (40% versus 85%). Extrapolating the mass-enhancement parameter for the significantly smaller penetration of the $n = 1$ image-potential state on Cu(001) (3%) yields $\lambda = 0.005$. Accordingly, for image-potential states on Cu(001) phonon broadening of the linewidth is below experimental resolution ($\Gamma^* = 2\pi\lambda k_B T < 1$ meV at 300 K). This will likewise hold for adsorbate-covered Cu(001).

As just mentioned, for the clean Cu(001) surface phonon contributions to quasielastic scattering are negligible. At this point there is thus no evidence that the microscopic origin of inelastic and quasielastic scattering processes is related. Note that for $n \geqslant 3$ the $(n + a)^{-3}$ dependence of the dephasing rate was *a priori* assumed. We expect that dephasing is a property related to the very surface. Consequently, surface defects, such as steps and adatoms will dominate quasielastic scattering rates. This and the relation between decay and dephasing of image-potential states will be illustrated in the following sections.
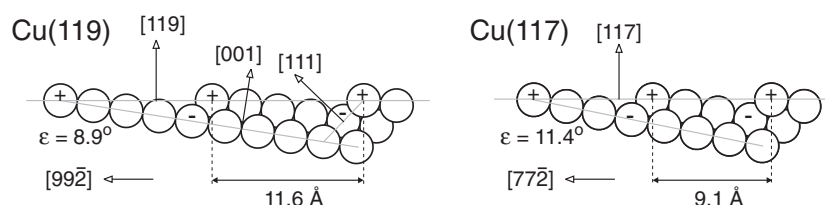
Figure 14. Hard sphere models of the bulk truncated Cu(117) and Cu(119) surfaces as projected on the (1$\bar{1}$0) plane (nearest neighbour distance $d_0 = 2.556$ Å).

4. Stepped surfaces—Cu(119) and Cu(117)

This section addresses the effect of steps, defects inherent to any surface in nature, by studying image-potential states on Cu(117) and Cu(119). As illustrated in figure 14 the stepped surfaces consist of (001)-terraces with mean width of 7/2 and 9/2 atoms. Densely packed steps of single-atom height run along the [$\bar{1}$10]-direction.

Prior to 2PPE we investigated the structure of Cu(117) by quantitative low-energy electron diffraction (LEED) [97]. The analysis reveals that the corrugation of the bulk truncated structure is essentially smoothed. The overall relaxation is considerable involving at least the top seven layers. Comparison with a LEED study of Cu(115) [98] indicates that this modification of the step shape is rather universal.

The morphology of stepped copper surfaces was characterized in detail by Giesen and co-workers using scanning tunnelling microscopy (STM) [99, 100]. For Cu(117) the distribution of steps is rather narrow and symmetrical about the mean terrace width. More than 50% of the steps are separated by 3.5 atoms, while distances of 2.5 and 4.5 atoms each contribute about 20% [101, 102]. With increasing terrace width this distribution broadens [103, 104].

4.1. Work function

Decrease of the work function on rough metal surfaces is commonly understood in terms of the Smoluchowski effect [105]. Smoothing of the electron density at steps and defects lowers the electron kinetic energy. The resulting spill-out of the charge at the surface leads to a perpendicular dipole moment which reduces the sample work function. The 2PPE setup is optimized for detection of electrons with low kinetic energy and sample work functions can be determined with high accuracy (± 5 meV) from the low-energy cut-off. As listed in table 2 the work function decreases with increasing step density. Applying the Helmholtz equation [106] yields a dipole moment of -0.024 D (1 Debye $= 0.208$ eÅ) per Cu step-edge atom. Similar small values have been observed for vicinal Cu(111) surfaces [107, 108] while values reported for stepped Pt(111) and Au(111) surfaces are about a magnitude larger (-0.6 and -0.25 D) [106, 109].

The data on copper agree well with calculations for steps on jellium [110]. For metals with d electrons like Pt, Au or Cu it was, however, argued that dipole moments will increase due to d-charge relocation at the step edge [110]. This effect may be compensated by electron attraction to the less well screened step-edge atoms as predicted *ab initio* for Al(111) [111].

In contrast to steps, single Cu adatoms on Cu(001) lead to a sizeable reduction of the sample work function[2]. Even without a microscopic model we can conclude that charge redistribution associated with steps on vicinal Cu(001) surfaces is noticeably weaker.

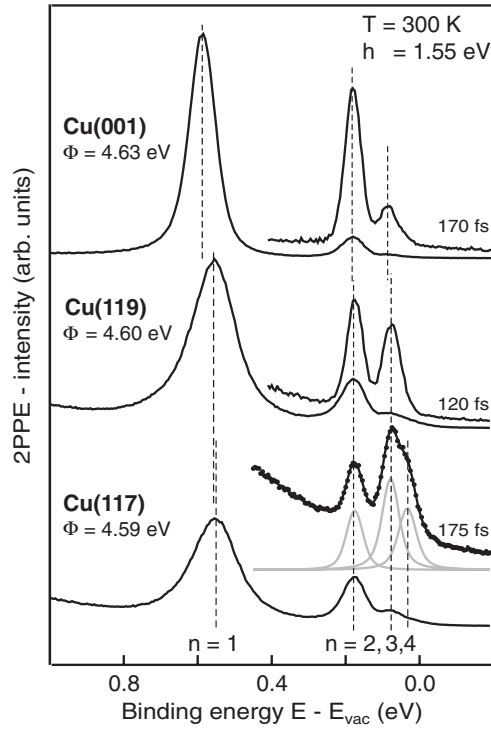[2] The initial slope in figure 26 yields a dipole moment of -0.28 D per adatom.

Figure 15. Energy-resolved 2PPE spectra for Cu(001), Cu(119) and Cu(117) recorded for normal emission. Relative intensity of $n = 2$ and 3 image-potential states is enhanced for spectra recorded with sufficient pump–probe delay.

4.2. Energies, dispersion and effective masses

Figure 15 compares energy-resolved spectra for Cu(001), Cu(119) and Cu(117) at $k_\parallel = 0$. Respective peak positions are gathered in table 2. Binding energies E_n for higher-image-potential states are calculated from the quantum beat periods in figure 18. On all three surfaces the series of image-potential states is best described introducing two quantum defects $a_1 > a_{\geqslant 2}$. Evaluating the work function via equation 14 agrees with the measured values within ± 5 meV. While binding energies on the stepped surfaces are related, we find a lowering of E_1 by about 40 meV when compared to Cu(001). Variations for higher image-potential states are within experimental error.

Surface corrugation can lead to electron confinement [112–114]. As known from the 'particle-in-a-box' problem, localization shifts the binding energy to lower values. Therefore a sound discussion requires us to specify the influence of the lateral corrugation on the dispersion $E_n(k_\parallel)$ [35]. Data for $k_\parallel$ running perpendicular to the step edge are depicted in figure 16. On the vicinal surfaces umklapp processes for $n = 1$ and 2 image-potential states occur in the SBZ. While the $n = 1$ parabola extends in the second SBZ, back-folding of the bands to the first SBZ is not resolved. The bottom of the image-potential-state bands is found at $k_\parallel = 0$, which corresponds to emission along the macroscopic surface normal. The zone boundary deduced from the dispersion (0.27 Å^{-1} for Cu(119) and 0.35 Å^{-1} for Cu(117)) coincides well with the values expected from the ideal step separation π/l. Superlattice effects for $n = 1$ have been previously observed by Wang *et al* on a potassium-stabilized Cu(119) surface [115]. Parallel
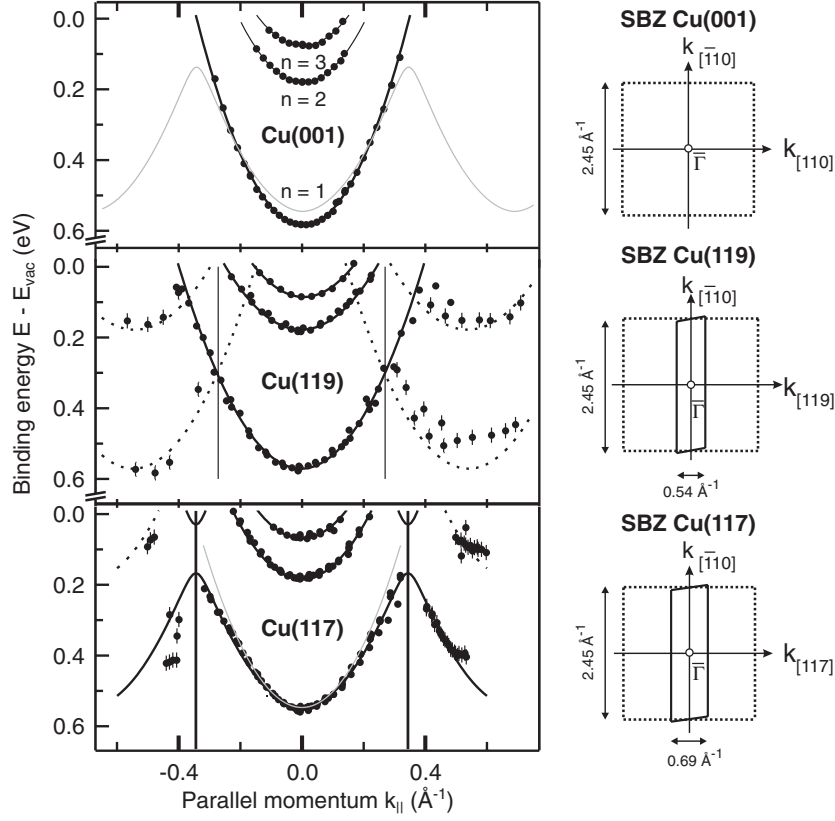
Figure 16. Energy versus in-plane momentum dispersion curves $E_n(k_\parallel)$ for Cu(001), Cu(119) and Cu(117) (see also [116]). Positive (negative) $k_\parallel$-values correspond to the direction running upstairs (downstairs) normal to the steps. Solid curves are fit results. Grey solid curves are interchanged between top and bottom panels to visualize different $E_n(k_\parallel)$. Vertical lines indicate boundaries of the SBZs sketched to the right.

to the steps the dispersion was found to equal that of the flat Cu(001) surface [115]. The band dispersion on Cu(119) is already well described by simple parabolas (for effective masses at the band bottom see table 2). The larger SBZ and likely higher degree of order for Cu(117) allow a more detailed analysis. Following [117] steps can be modelled by one-dimensional potential barriers. Transmission through the step barriers at distances l is described by a complex coefficient $T = |T| \exp(i\varphi)$. This yields the dispersion relation for $k_\parallel$ running normal to the step edge [117]

$$E(k_\parallel) = \frac{\hbar^2}{2m^*l^2}[\arccos(|T|\cos(k_\parallel l)) - \varphi]^2 - E_n^0, \tag{15}$$

where m^* and E_n^0 correspond to the effective mass and binding energy at the band bottom of the flat surface. $T = 1$ gives the free-electron parabola. For $|T| < 1$ the band bottom shifts to lower binding energy and the effective mass increases close to the SBZ zone edge.

Applying equation (15) to describe the dispersion of the $n = 1$ image-potential state on Cu(117) we obtain $|T| = 0.96 \pm 0.02$, $\varphi = -(0.027 \pm 0.01)\pi$ and $E_1^0 = 550 \pm 10$ meV. The agreement between data and fit (solid curve in figure 16, bottom panel) is quite convincing. A simple parabolic fit does not allow us to equally well reproduce the dispersion. While
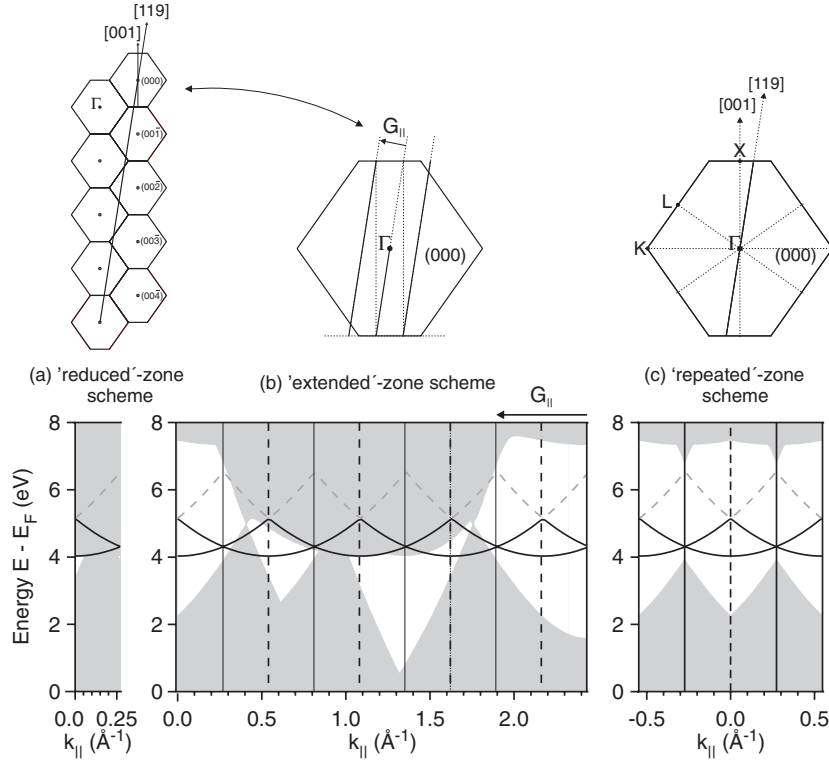
Figure 17. Projected bulk band structure of Cu(119). (a) 'Reduced'-zone scheme, (b) 'extended'-zone scheme and (c) 'repeated'-zone scheme including only states from (b) for $|k_\parallel| \leqslant G_\parallel/2$. The sampling of bulk states is indicated on top for $k_\parallel = 0$.

the curvature at the band bottom is best described by $m_1^*/m_0 = 0.86 \pm 0.03$, we obtain $m_1^*/m_0 = 1.04 \pm 0.03$ including higher $k_\parallel$-values. This increase signals a finite mini-gap at $G_\parallel/2$. The above parameters result in a width of 135 meV[3]. For the $n = 2$ and 3 image-potential states the accessible $k_\parallel$-range is too small to apply a similar analysis and data are well described by simple parabolas.

The step potential contributes only $\leqslant 5$ meV to the shift of the $n = 1$ band bottom indicating that the difference to the flat surface is not caused by lateral confinement[4]. So far we have neglected any change of the surface-projected bulk band structure. As illustrated in figure 17 for Cu(119) the projection is obtained by sampling all states with $k_\perp$ along the [119]-direction for fixed $k_\parallel$. Strictly elaborated this leads to the 'reduced'-zone scheme with a substantially downsized surface-projected bulk bandgap. The closing of the gap would result in an increased overlap of the image-potential-state wavefunction with bulk states, i.e. a transition from surface state towards surface resonance. Among other effects this should lead to increased dephasing due to enhanced electron–phonon coupling which is, however, not observed (section 4.3).

An alternative approach emerges by unfolding the surface-projected bulk band structure in contributions of individual bulk Brillouin zones. Such an 'extended'-zone scheme can be constructed by sampling states in the bulk Brillouin zone (000) along rods in the [119]-direction

---

[3] Applying the step-intrinsic transmission coefficient T we expect for Cu(119) a mini-gap of ≈ 80 meV compatible with the peak broadening observed at the SBZ zone edge.

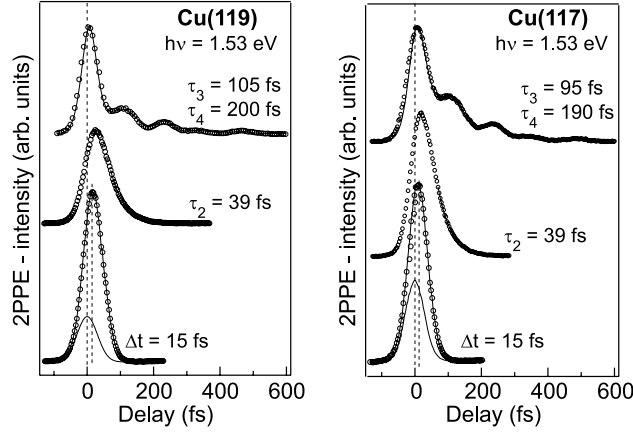[4] For a discussion on the $n = 0$ surface state see also [114].

Figure 18. Time-resolved 2PPE measurements for Cu(119) [47] and Cu(117).

connected by reciprocal lattice vectors of the lateral superlattice $G_\parallel$ (figure 17(b)). Sampling adjacent bulk Brillouin zones (e.g., (000) and (00$\bar{1}$)) corresponds to an umklapp process. Neglecting higher-order scattering processes, as suggested by the reduced intensity of the back-folded bands and the disorder of the step-induced superlattice, leads to a model including only $k_\parallel$-values within the first SBZ. In this case a sizeable bandgap appears at $k_\parallel = 0$. Compared to Cu(001), the centre of the gap is at higher energies and according to the phase analysis model [77, 87] this shift alters the image-potential-state binding energies. Applying the values to figure 18 of [21] yields a reduction of 30 and 5 meV for E_1^0 and E_2^0 on Cu(119) in reasonable agreement with the measured values (40 and 10 meV).

I conclude that the binding energy shift is due to a modification of the surface-projected bulk band structure on the stepped surfaces and lateral confinement is insignificant [116]. Additional strong localization of the image-potential state at the step edge, as observed with inverse photoemission [118], is not confirmed by 2PPE [35]. The image-potential states react to the step potential in the way expected for Bloch states. The propagation is along the average surface obeying the periodicity $E(k_\parallel) = E(k_\parallel + G_\parallel)$. $G_\parallel$ corresponds to a reciprocal lattice vector of the respective superlattice. This symmetry confirms that $k_\parallel$ is conserved with respect to the average surface plane and indicates a coherent wavefunction of the image-potential state extending over several terraces.

4.3. Population and phase relaxation

Time-resolved measurements for Cu(117) and Cu(119) at $k_\parallel = 0$ are depicted in figure 18. The decay rate Γ_1^0 of the short-lived $n = 1$ image-potential state is seen as an offset to the cross-correlation trace (dashed curve in figure 18). Decay rates of higher states are evaluated by the exponential decay of the signal after the cross-correlation trace (Γ_2^0) and within the framework of multilevel optical Bloch equations (Γ_n^0, $n = 3, 4, 5$). Results are gathered in table 2. The overall larger decay rates on the stepped surfaces are attributed to the narrowing of the Cu(001) gap near the X point when projected along the [119] and [117] directions, respectively. As seen in figure 17 this leads to an increase of unoccupied bulk states serving as decay channels in inelastic electron–electron scattering. In addition, interband decay $|n + 1\rangle \rightarrow |n\rangle$ is enhanced on the stepped surfaces thereby enlarging decay rates for $n \geqslant 2$ (see section 4.5).

Decay of the quantum beat pattern is well described neglecting dephasing ($\Gamma_{34}^* = \Gamma_{45}^* \leqslant$ 2 meV). Dephasing rates for lower image-potential states are evaluated from energy-resolved
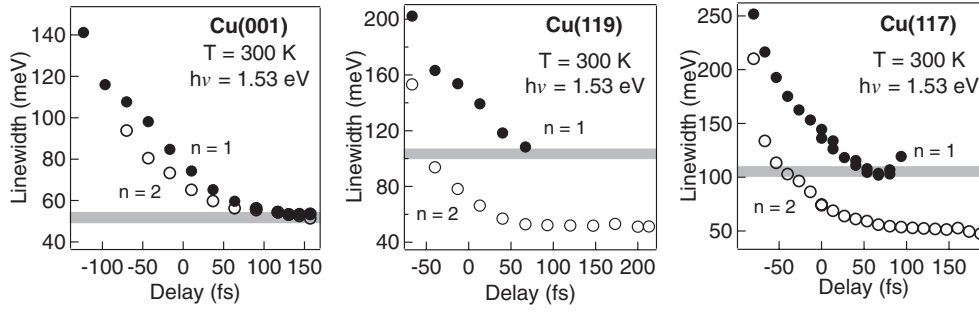
Figure 19. Linewidths of the $n = 1$ (filled circles) and 2 (open circles) image-potential states on Cu(001) [43], Cu(119) [116] and Cu(117) as a function of pump–probe delay.

spectra (figure 19). The linewidth of the $n = 2$ image-potential state exhibits nearly the same dependence on pump–probe delay as the $n = 1$ state on Cu(001), i.e. $\Gamma_2^* \leqslant 5$ meV. In contrast the $n = 1$ linewidth increases on both stepped surfaces. Following the analysis in section 2.3.2 yields a dephasing rate Γ_1^* of 40 ± 5 meV. Besides quasielastic scattering, linewidth broadening may be caused by surface inhomogeneity. Comparison of the shifts obtained from the phase-analysis model (30 meV) and the finite transmission $|T|$ ($\leqslant 5$ meV) with the experimental shift (40 meV) yields an upper limit for inhomogeneous broadening of 10 meV. Thus the 80 meV Lorentzian linewidth contribution of the $n = 1$ state is primarily a signature of quasi-elastic scattering events ($2\Gamma_1^*$) and the modelling by Bloch equations is adequate. We note furthermore that linewidths coincide at 100 and 300 K. This suggests that electron–phonon scattering is insignificant and that the bulk penetration of the image-potential-state wavefunctions on the vicinal surfaces is small, i.e. matches that on flat Cu(001). In other words dephasing is indeed caused by the steps. Dephasing vanishes for perfect order [7]. Thus only surface imperfections, i.e. the finite terrace width distribution, will provoke quasielastic scattering events [116].

Since dephasing for higher-image-potential states is negligible one may yet conclude that the step dipole potential rapidly drops off in front of the surface and therefore influences only electron scattering close to the surface ($n = 1$, see figure 9). However, umklapp processes are observed for $n = 2$ and we will see in the following section that the dynamics of all image-potential states is significantly altered in the presence of steps. So far we have only discussed decay rates Γ_n^0 at $k_\parallel = 0$, i.e. the band bottom. Now we consider the dynamics of electrons with finite parallel momentum.

4.4. Momentum dependence of the dynamics

4.4.1. Intraband decay—$k_\parallel$ dependence of lifetimes. The energy range of excited intermediate states is determined by the photon energy of the pump pulse and the Fermi level, respectively. At a fundamental photon energy of $h\nu = 1.53$ eV intermediate states up to $3h\nu = 4.59$ eV above E_F, i.e. close to the vacuum level of the copper surfaces studied, are accessible. Note that scattering between excited electrons is irrelevant for the dynamics, since even if each photon of a single pulse excites an electron into the image-potential-state band the density is still below 10^{11} cm^{-2}.

The decay rate Γ_n at finite momentum ($k_\parallel \neq 0$) is thus governed by the number of unoccupied states which increase with parallel momentum. Kliewer *et al* [23] were the first to demonstrate that besides decay into bulk states decay within the surface band opens a new, very efficient decay channel. The overlap of wavefunctions of states belonging to the same
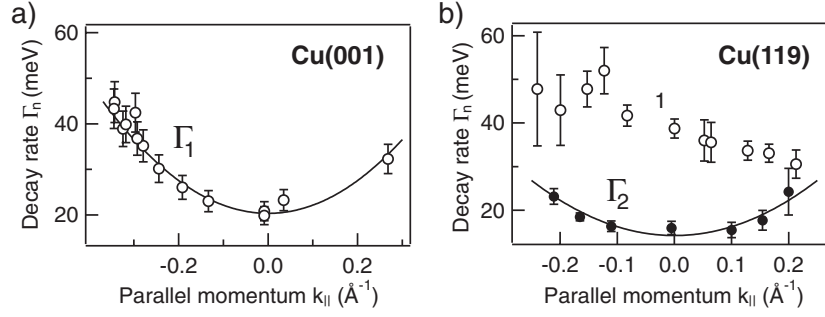
a)

b)

Figure 20. Decay rate Γ_n as a function of parallel momentum for (a) $n = 1$ on Cu(001) and (b) $n = 1$ and 2 on Cu(119) [35]. $k_\parallel > 0$ corresponds to the direction running upstairs. The errors indicate the relative uncertainties within the series of measurements. For absolute errors see table 2.

band is sufficiently higher than the overlap with bulk states. Therefore intraband decay can even dominate decay rates at $k_\parallel \neq 0$. Recently Berthold *et al* observed a linear increase of the decay rate with energy above the band bottom E_n^0 for the $n = 1$ and 2 image-potential states on Cu(001) [119]. Many-body theory revealed that intraband scattering contributes about 50% to the increase $d\Gamma/dE$.

This behaviour is illustrated in figure 20(a). For the $n = 1$ image-potential state on Cu(001) the $k_\parallel$-dependence of the decay rate is symmetric and roughly parabolic. We find $d\Gamma_1/dE = 44 \pm 10$ meV eV^{-1} in excellent agreement with the value in [119].

Decay rates on Cu(119) are shown in figure 20(b). For the $n = 2$ image-potential state the $k_\parallel$-dependence of the decay rate is again symmetric. Since decay rates Γ_1^0 on Cu(001) and Γ_2^0 on Cu(119) roughly coincide we expect similar curvatures $\propto d\Gamma/dE$. The somewhat large value $d\Gamma_2/dE = 53 \pm 20$ meV eV^{-1} is attributed to an increase of bulk decay channels on Cu(119) and may be rationalized by the surface-projected bulk band structure in figure 17. Compared to Cu(001) the gap on Cu(119) is narrower. Consequently the number of bulk decay channels increases more strongly with $k_\parallel$ and so does the decay rate.

For the $n = 1$ image-potential state the dynamics are more intricate: electrons running upstairs ($k_\parallel > 0$) live apparently longer than those running downstairs. This asymmetry and in particular the decrease of the decay rate for positive momenta cannot be motivated within the band-structure model. The symmetry $E(k) = E(-k)$ rules that bulk and intraband decay channels for electrons with momentum $k_\parallel$ are identical to those with momentum $-k_\parallel$. The $k_\parallel$-dependent decay rate thus points to an asymmetry in the scattering process at the step potential and we will clarify its nature in the following section.

4.5. Interband decay

Figure 21(a) depicts sets of energy-resolved spectra for Cu(119) at the band bottom ($\vartheta = 0°$) and for parallel momenta close to the SBZ edge ($\vartheta = 28°$, $G_\parallel/2 \approx 0.27$ Å^{-1}). Each set contains from top to bottom spectra measured at $T_d = 35, 70$ and $100(125)$ fs pump–probe delay, respectively.

The high-intensity peak in the spectra measured at $T_d = 35$ fs is associated with the $n = 1$ image-potential state and we resolve the lower and upper branches (LB and UB) of the $n = 1$ band in the second SBZ[5]. Peak positions are shown as solid black circles in figure 21(b).

---

[5] For $\vartheta > 36°$ emission from the UB is cut at the high-energy side, since the maximum kinetic energy is restricted by the photon energy of the pump pulse $3h\nu$.
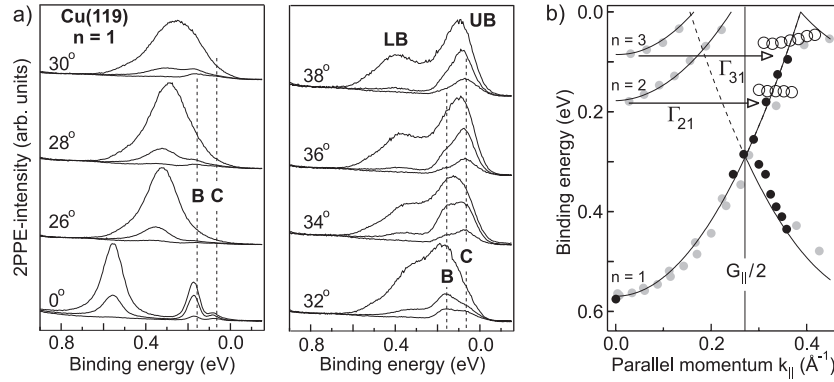
Figure 21. (a) Sets of energy-resolved spectra for Cu(119) and emission angles close to the SBZ edge $\vartheta \approx 28°$ [35]. Each set contains from top to bottom three spectra measured at $T_d = 35, 70, 100$ fs (125 fs for $\vartheta \geqslant 34°$). Intensity above $E_{vac} = 0$ is close to zero in all spectra. (b) Energy versus in-plane momentum dispersion curves $E(k_{\|})$ for Cu(119). Solid circles indicate peak positions taken from the spectra in (a) for the $n = 1$ image-potential state determined at 30 fs delay and peaks B and C determined at 70 and 100 fs delay, respectively. The solid arrows show interband-scattering paths (Γ_{21} and Γ_{31}) from the bottom of $n = 2$ and 3 image-potential-state bands in the first SBZ to the upper branch of the $n = 1$ image-potential-state band in the second SBZ.

Spectra change considerably for larger delay between pump and probe pulses. The LB signal of the $n = 1$ image-potential state depends on direction. Emission intensity in the first SBZ (26°) persists significantly longer than in the second SBZ ($\vartheta \geqslant 36°$). Noting $E(k_{\|}) = E(k_{\|} - G_{\|})$ this corroborates that electrons running upstairs live apparently longer than those running downstairs.

Two new, obviously long-lived components marked B and C become visible for $T_d \geqslant 70$ fs. As seen from figure 21(b) (open circles), the position of peak B is independent of emission angle while peak C exhibits a slight shift to lower binding energies. Peak B exhibits maximum intensity for $\vartheta \approx 32°$. With increasing angle and thus parallel momentum peak C gains weight reaching its maximum at $\vartheta \approx 36°$. The corresponding parallel momenta each coincide with the parabola of the $n = 1$ band. Comparison to the spectrum recorded at $\vartheta = 0°$ reveals that the binding energy of peaks B and C is about 40 meV smaller than at the bottom of the $n = 2$ and 3 image-potential-state bands. With increasing pump–probe delay the intensity of peak C outweighs that of peak B.

The decay rates of B and C are obtained from time-resolved measurements following the $n = 1$ upper branch in the second SBZ. Data are shown after background subtraction on a semi-logarithmic scale in figure 22. Spectra from bottom to top correspond to decreasing binding energy and thereby trace states with increasing momentum ($k_{\|}$ running upstairs). Depending on the binding energy the signal contains three components (I, II, III). Decay rates and percentages depicted in figure 23 were evaluated by decomposing the spectra into exponential decaying contributions starting at delay zero. For binding energies $E > 300$ meV we mainly observe a fast-decaying component (I) in accordance with decay of the $n = 1$ image-potential state after direct population of the upper branch by the pump pulse.

The decay rate $\Gamma_{II} = 19 \pm 3$ meV of component II is only slightly larger than that of the $n = 2$ image-potential state at $k_{\|} = 0$ ($\Gamma_2 = 17 \pm 2.3$ meV, dashed horizontal line). The onset of component II can quite well be described by a Gaussian centred at an energy $E_2^0 - 80$ meV with maximum contribution of about 80% and a width of 125 meV. This suggests
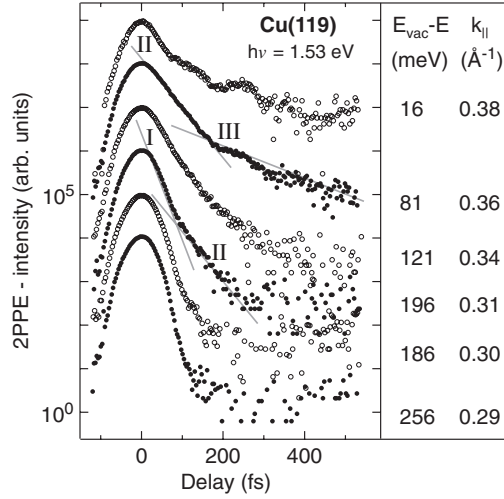
Figure 22. Time-resolved 2PPE measurements of the $n = 1$ image-potential state on Cu(119) plotted on a semi-logarithmic scale [35]. Spectra are recorded for $k_\parallel$ running upstairs. Components I, II and III are indicated by grey solid lines.
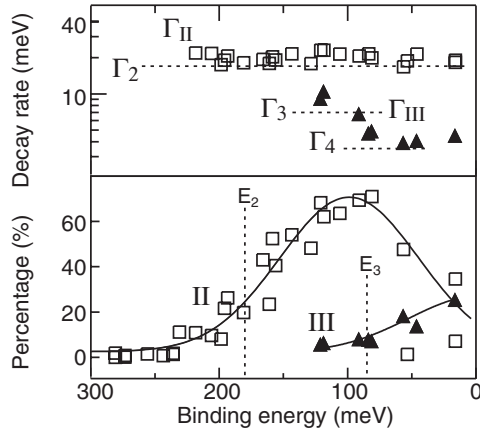

Figure 23. Decay rates and percentages of components II and III [35].

that component II and thereby peak B stem from electrons originally excited to the $n = 2$ band and subsequently scattered to the $n = 1$ image-potential-state parabola. The time-resolved spectrum at a binding energy of 121 meV reveals that at $k_\parallel = 0.34$ Å^{-1} population decay in the $n = 1$ band is almost entirely governed by Γ_{II}, i.e. the decay of the population in the $n = 2$ band. The excitation probabilities for image-potential states scale roughly as the decay rate. This yields $\Gamma_2/\Gamma_1 \approx 0.38$ and suggests that interband decay ($|2\rangle \rightarrow |1\rangle$) is rather efficient. At somewhat lower binding energies this scattering contribution levels off as seen from both energy- and time-resolved spectra. Remember that the photon energy of the pump pulse is 4.59 eV which ensures excitation of states all the way up to $E_{vac} = 0$. Furthermore, it seems unlikely that interband decay from states above the band bottom becomes less probable. As discussed already in the last section the image-potential-state band itself provides a rather efficient decay channel for electrons excited to states with $k_\parallel \neq 0$. Thus with increasing time

after the pump pulse electrons will accumulate at the $n = 2$ band bottom and thus enhance the contribution at energies close to E_2^0. In addition decay into bulk states increases with parallel momentum. Close inspection of peak positions at 70 fs delay reveals that for emission angles up to $34°$ the $n = 1$ signal is shifted to lower energies by 35 ± 10 meV as compared to spectra recorded at 30 fs delay. This peak shift is again a signature of time-dependent redistribution of electrons, i.e. intraband decay within the $n = 1$ image-potential-state band.

More noticeably, the peaklike shape of B implies that interband scattering $|2\rangle \rightarrow |1\rangle$ has to be quasielastic, i.e. involves only negligible energy transfer. Naïvely we would expect peak B at energy E_0^2, i.e. the bottom of the $n = 2$ band. The observed upward shift is attributed to finite angular resolution. In first-order approximation such a broadening vanishes for $\nabla E(k_\parallel) = 0$. This holds for $k_\parallel = 0$, i.e. at the band bottom. Due to interband scattering the population of the $n = 2$ band is, however, probed at $k_\parallel \neq 0$, where finite angular resolution leads to an asymmetric broadening and a shift of the maximum above E_2^0. This likewise explains the shape of curve II and the somewhat larger decay rate Γ_{II}. While interband scattering $|2\rangle \rightarrow |1\rangle$ will start at energy E_2^0, finite resolution broadens the onset, and shifts the maximum to higher energies. Tracing thereby states at energies $E > E_2^0$ adds decay rates $\Gamma > \Gamma_2$.

Following the above discussion, contribution III and thereby peak C is ascribed to interband scattering from $n = 3$ and higher-image-potential states into the $n = 1$ band. The decrease of the decay rate Γ_{III} with decreasing binding energy is attributed to successively sampling more states of the Rydberg-like series via interband scattering when moving up the $n = 1$ band. This contribution of higher-image-potential states is also revealed by the slight shift of peak C to smaller binding energies with increasing $k_\parallel$. For sufficiently high energies a quantum beat pattern is seen in the time-resolved spectra (figure 22 top). The period of 115 ± 10 fs corresponds to quantum beats between $n = 3$ and 4 states. The occurrence of quantum beats can be readily understood by noticing that interband transitions between $n = 1$ and higher-image-potential states will predominantly occur at the surface, where the $n = 1$ image-potential state has its maximum probability density. Thus the oscillatory motion of the electron perpendicular to the surface is probed, as in quantum beat experiments on Cu(001) [6], via interband scattering occurring mainly at the surface.

I conclude that peaks B and C are caused by quasielastic scattering with large momentum transfer, whereby electrons from states close to the bottom of the $n = 2$ band (peak B) and higher-image-potential-state bands (peak C) in the first SBZ are scattered to the upper branch of the $n = 1$ image-potential-state band in the second SBZ. The interband-scattering path is schematically indicated by arrows (Γ_{21} and Γ_{31}) in figure 21(b). Such a scattering process has recently been observed by Berthold *et al* in time-resolved measurements for clean Cu(001) and likewise explained as resonant interband scattering between higher states and the $n = 1$ image-potential-state band [36]. The actual origin of the interband-scattering process on the nominal flat surface remained however unclarified.

4.6. Asymmetry in interband decay—quasielastic scattering at steps

Time-resolved spectra of the $n = 1$ image-potential state for $k_\parallel$ running upstairs (solid circles) and downstairs (open circles) are compared in figure 24. This immediately reveals an enormous asymmetry. At binding energies $\leqslant 180$ meV we see component II mainly for $k_\parallel$ running upstairs. Scattering $|2\rangle \rightarrow |1\rangle$ in the downstairs direction contributes only 6% to the time-resolved signal which has to be compared to the value of 70% derived for $k_\parallel$ running upstairs. In other words interband scattering is merely observed for positive momentum transfer. This is the reason why interband-scattering paths to states with group velocity $v < 0$ have been omitted in figure 21(b).
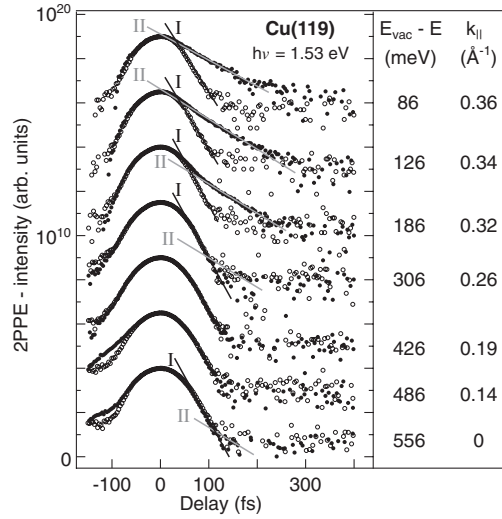
Figure 24. Time-resolved 2PPE measurements of the $n = 1$ image-potential state on Cu(119) [35]. Spectra are recorded for $k_\parallel$ running either upstairs (solid circles) or downstairs (open circles).

The significant asymmetry proves that interband scattering is indeed caused by the steps. For a perfectly ordered surface and neglecting phonon contributions quasielastic scattering will not occur (see also section 5.3). Thus the origin of interband scattering is attributed to surface disorder, i.e. the finite terrace-width distribution and, less likely, also step roughness. Typical momentum transfer in interband scattering on Cu(117) and Cu(119) is approximately $G_\parallel/2$, which corresponds in real space to the distance between every second step $2 \cdot l$. Thus I expect $2 \cdot l$ correlations to be essential for disorder-induced interband scattering on the vicinal surfaces. STM experiments to question such correlations are under way. In addition the asymmetry of the interband-scattering process proves that the detailed shape of the scattering potential is of vital importance. Simply considering the dipole at the step edge (see figure 14) is not sufficient. Parallel to the surface the electron would be accelerated in the downstairs direction in contrast to the observations. Detailed modelling of the process asks obviously for a self-consistent calculation of the image potential at the step. Even a phenomenological description using Bloch equations needs as input the complete $k_\parallel$-dependence of the interband-scattering process. Since interband scattering is asymmetric the isotropic rate equation model used in [36] is inappropriate.

The considerable asymmetry seen for Cu(119) is also observed for Cu(117). The maximum percentage of interband scattering $|2\rangle \rightarrow |1\rangle$ for $k_\parallel$ running upstairs is, however, significantly smaller ($\approx$25%). As seen from figure 16 for both vicinal surfaces momentum transfer associated with interband scattering is comparable. Thus the different percentages of interband decay may be explained by different terrace-width distributions on Cu(117) and Cu(119), i.e. different degrees of order. In addition on Cu(117) the number of final states available for interband scattering is smaller due to the wider mini-gap.

Since interband scattering between different states is sizeable, intraband scattering ($|-k_\parallel\rangle \rightarrow |k_\parallel\rangle$) within the $n = 1$ band may be even more likely. In this case the direction dependence in the scattering process leads to a redistribution of electrons on the image-potential-state parabola. States with momentum running upstairs become populated at the cost of states with momentum running downstairs. This explains the direction dependence of the decay rate of the $n = 1$ image-potential state.
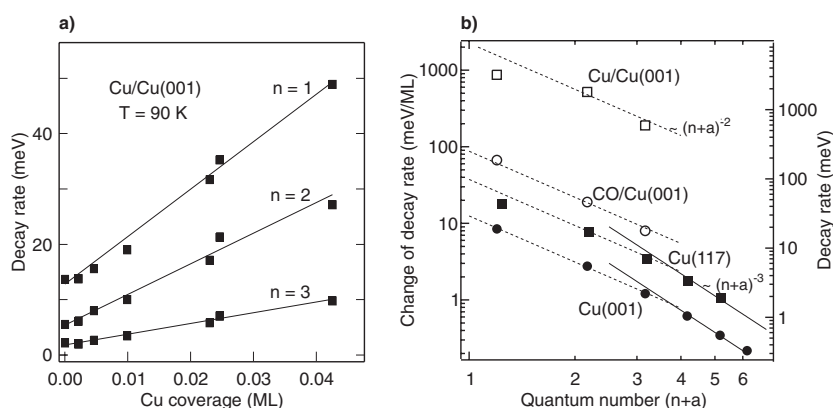
Figure 25. (a) Decay rate of the $n = 1, 2$ and 3 image-potential states on Cu(001) as a function of Cu coverage. (b) Change of decay rate with coverage for Cu/Cu(001) and CO/Cu(001) (open symbols) and decay rate for clean Cu(001) and Cu(117) (filled symbols) as a function of quantum number $(n + a)$ [26].

5. The influence of adsorbates

For the Cu(001) surface an electron in an image-potential state is almost entirely located in front of the surface. Already evident from the results on the stepped surfaces the dynamics is strongly influenced by surface disorder. In this section I will review the influence of adsorbates on decay and dephasing. First we consider small coverage, where adsorbates can be viewed as single, uncorrelated defects. In the second part the relation between surface order and dephasing is established.

Decay rates presented are solely measured at $k_\parallel = 0$. For the $n = 1$ image-potential state the decay rate is evaluated with respect to the signal of the occupied surface state on Cu(111), since the system used has a cross-correlation of 95 fs [10]. For this purpose both Cu samples are mounted on a sample holder which allows us to heat the samples separately. All measurements are performed at a sample temperature of 90 K. After deposition of Cu, the Cu(001) sample was slightly annealed to 115 K to avoid further diffusion and achieve stable conditions during the measurement [120]. Smoother films were prepared by step-wise annealing up to 400 K for 1 min.

5.1. Defect-induced decay

As an example for isolated defects let us look at the influence of small numbers of Cu adatoms adsorbed at 90 K on Cu(001) [63]. At this temperature the mobility of Cu is very low and we can assume an uncorrelated distribution of adatoms on the surface [121–124]. As shown in figure 25(a) the decay rates for the $n = 1, 2$ and 3 image-potential states are found to increase linearly with Cu coverage with the slope depending on the quantum number n (figure 6 in [47]). The slope is referred to as change of decay rate (with coverage). A linear increase with adsorbate coverage was also found for low coverage of CO molecules on Cu(001) [7, 47].

In figure 25(b) the change of decay rate with coverage $d\Gamma_n/d\Theta$ for the adsorbate systems is compared to the decay rate found on the clean Cu(001) and the vicinal Cu(117) surfaces. The different scales on the ordinates have been linked assuming a defect density of 0.48/3.5 (1/monolayer) for Cu(117) ($\approx 48\%$ of terraces do not exhibit a step separation of 3.5 atoms [99]). The abscissa is used to order the results as a function of the quantum number $n + a$. Most
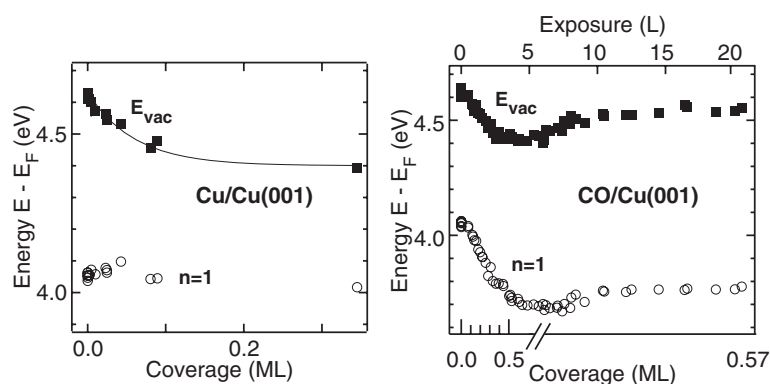
Figure 26. Vacuum energy E_{vac} and energy of the $n = 1$ image-potential state for Cu/Cu(001) (left panel) and CO/Cu(001) (right panel) as a function of coverage.

notably, the change of decay rate with coverage is more than one order of magnitude larger for Cu adatoms as compared to CO molecules. For the clean surface and $n \leqslant 3$ the decay rate scales roughly as $(n+a)^{-2}$ (dashed straight line). The change of decay rate for CO molecules reproduces this trend. In contrast, for Cu adatoms the change of decay rate shows a trend as the decay rate on Cu(117).

The change of decay rate with adsorbate coverage may be explained by (a) an increase of inelastic decay channels and (b) an increase of disorder, which causes quasielastic scattering with large momentum transfer.

(a) The linear increase of the decay rate with coverage can be linked to a linear increase of additional decay channels introduced by the adsorbates [7]. For CO such additional unoccupied states in the bandgap have been identified by inverse photoemission [125, 126] and they might indeed serve as final states for inelastic decay. Change of decay rate for CO/Cu(001) is well described by simply scaling the decay rates on Cu(001) by a common factor.

(b) This suggests that interband scattering is not significantly enhanced upon CO adsorption. In contrast, the change of decay rate for Cu adatoms on Cu(001) shows the trend observed for the decay rate on Cu(117). For the vicinal surfaces interband scattering contributes sizeably to decay of $n \geqslant 2$ image-potential states. It is therefore likely that interband scattering is an important mechanism for decay of $n \geqslant 2$ image-potential states upon Cu adsorption on Cu(001).

What causes the difference between CO molecules and Cu adatoms? I propose it is the nature of the scattering potential, i.e. distinct strength and shape.

As seen from figure 26 for CO on Cu(001) the energy of the $n = 1$ image-potential state decreases relative to E_F for small coverage. In contrast an increase is observed for Cu on Cu(001) (see figure 26) [10]. This suggests that electrons in the image potential experience an attractive potential for CO molecules but a repulsive potential for Cu adatoms. As in the case of steps a quantitative understanding of electron scattering certainly requires calculations.

Decay of electrons in the $n = 1$ image-potential state is not governed by interband scattering. But refilling of state $n = 1$ at $\overline{\Gamma}$ from higher-image-potential states via interband scattering and successive intraband decay can occur [36]. It seems not very likely that the large change of decay rate of the $n = 1$ image-potential state upon Cu adsorption is solely governed by inelastic decay into bulk and adsorbate-induced states. Since quasielastic scattering with
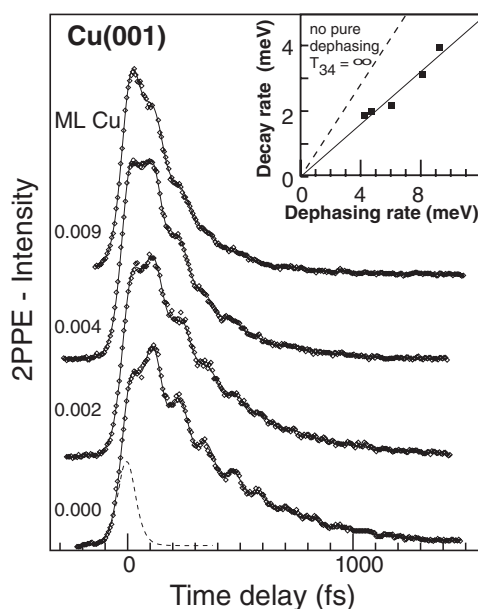
Figure 27. Time-resolved measurements for Cu on Cu(001). The coherent excitation of the $n = 3$ and 4 image-potential states leads to quantum beats superimposed on the observed decay of the $n = 3$ population. The inset compares population decay and dephasing rate. The dashed line indicates the expected trend in the absence of pure dephasing [63].

large momentum transfer into bulk states can equally well reduce the population in the $n = 1$ image-potential state, I suggest this decay mechanism to be operative. Experiments to test these assertions are under way.

5.2. Defect-induced dephasing

The enhancement of quasielastic scattering events with small momentum transfer by defects is best illustrated for the higher-image-potential states $n \geqslant 3$. Here the information on both decay and dephasing rates can be gained from coherent spectroscopy [6, 7, 10, 63]. As described in section 2.3.3 the excitation of several image-potential states leads to a quantum beat pattern superimposed on the exponential decay of the signal. When tuning the analyser to the $n = 3$ image-potential state on the clean Cu(001) surface we obtain the spectrum at the bottom of figure 27. While the signal decays on a timescale of $\tau = 330$ fs the amplitude of the oscillations decays on a slightly smaller timescale of $T_{osc} = 280$ fs [7]. For this interference pattern to be observed a fixed phase relation between the $n = 3$ and 4 image-potential-state wavefunctions is essential. As already discussed the total dephasing time T_{osc} contains not only contributions from inelastic decay Γ but also from quasielastic scattering processes Γ^*. After the cross-correlation trace (dashed line in figure 27) T_{osc} does involve only scattering of the electron in the intermediate state and is given by equation (12) [7].

A few thousandths of a monolayer of Cu adatoms are sufficient to significantly decrease both the decay time of the overall signal and the amplitude of the oscillations [63]. As shown in the inset of figure 27 decay and dephasing rates increase proportionally. In the absence of pure dephasing contributions ($\Gamma^* = 0$) we would obtain the dashed line. This demonstrates that pure dephasing and decay are of similar magnitude. As already shown in figure 5 (section 2.3.3)
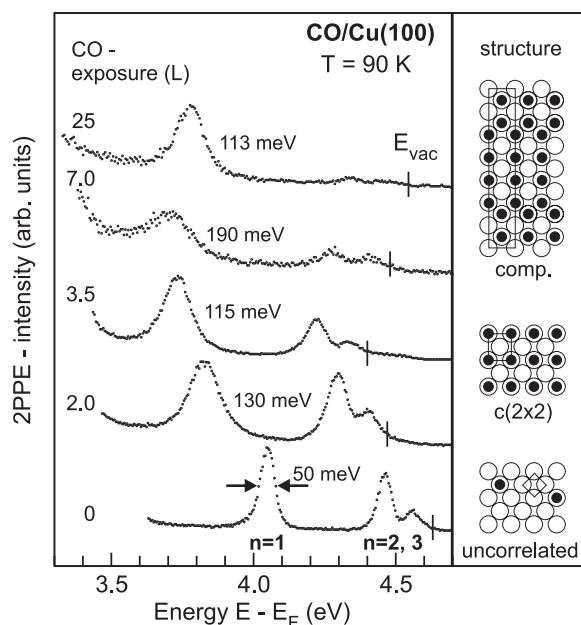
Figure 28. Series of energy-resolved 2PPE spectra as a function of CO exposure [7].

comparable pure dephasing rates are observed for CO molecules on Cu(001) [10]. In contrast the decay rate of the population is nearly unaltered at this very low CO coverage (see inset of figure 5).

For the $n = 1$ and 2 image-potential states quantum beat patterns are not observed, but as discussed in section 2.3.2 the same information can be extracted from linewidth analysis. It turns out that for sufficiently low coverage the dephasing rate increases again linearly with coverage [10, 63]. Since there is no evidence for lateral localization of the electron in the image-potential state and an uncorrelated distribution of adsorbed Cu atoms and CO molecules is expected at low coverage, I neglect possible contributions from inhomogeneous broadening. The linear dependence on adsorbate coverage allows us then to evaluate the change of dephasing rate with coverage.

5.3. Regaining surface order

Besides illustrating different decay mechanisms induced by defects, the adsorbate systems studied allow us to correlate surface order to dephasing and decay [7, 63]. In figure 28 a series of energy-resolved spectra of the $n = 1$, 2 and 3 image-potential states is depicted. In contrast to the linear increase at low coverage, the linewidth of the $n = 1$ image-potential state varies non-monotonically for higher CO exposures. Minima of the linewidth are found at 0, 3.5 L and saturation exposure. For these exposures ordered surface structures (1×1), $c(2 \times 2)$ and $c(7\sqrt{2} \times \sqrt{2})R45°$ are formed. In figure 29 decay rate and inverse linewidth are compared to the width of superstructure spots observed in LEED.

We do not observe a correlation of decay rate with LEED spotwidth. In contrast, linewidth and LEED spotwidth exhibit a similar coverage dependence. I again argue that the electron in the image-potential state samples over a considerable surface area, so that inhomogeneous broadening is small. Then the correlation between linewidth and spotwidth supports the picture
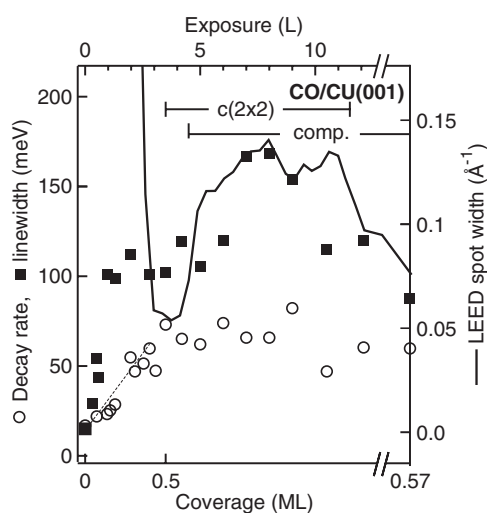
Figure 29. Decay rate (open circles), linewidth (solid squares) and LEED superstructure spot width (solid curve) for the $n = 1$ image-potential state on Cu(001) as a function of CO exposure (see also [7]). The coverage for the ordered structures is given at the bottom in monolayer units of the clean Cu(001) surface.

where pure dephasing is caused by quasielastic scattering of the electron in the intermediate state. For less-ordered overlayers the increase in spotwidth is caused by scattering events with small momentum transfer. Small momentum change will likewise give rise to dephasing of an electron in the image-potential state [7].

A somewhat different situation is found for Cu homoepitaxy [63]. As quasi-layer-by-layer growth is observed already at low temperatures [127], surface order oscillates with Cu coverage. As expected, upon completion of one monolayer the linewidth and decay rate of the $n = 1$ image-potential state decreases. The comparable decrease of the decay rate and dephasing rate upon completion of a monolayer for Cu on Cu(001) indicates that inelastic decay via scattering involving large momentum transfer and quasielastic scattering with small momentum transfer are related.

6. Comparison of decay and dephasing rates for steps and adsorbates

In the previous sections several examples for decay and dephasing of image-potential states have been presented. As expected atoms, molecules and steps at the Cu(001) surface all affect the dynamics of the electron in the image-potential state. The dependence on the distance of the electron in front of the surface and on the overlap with continuum states is probed by studying image-potential states with increasing quantum number n.

We can now seize the relative magnitude of quasielastic and inelastic scattering for the different systems studied. In figure 30 the dependence on the quantum number $(n + a)$ is compiled for the stepped Cu(119) surface and the two adsorbate systems studied. Data for Cu(117) are comparable to the results on Cu(119). The branching ratio is a term independent of coverage or surface morphology. The individual contribution of the $n = 3$ image-potential state was evaluated assuming an $(n + a)^{-3}$ dependence of the dephasing rates for $n = 3$ and 4. While this introduces some arbitrariness it does not substantially alter the general trend observed.
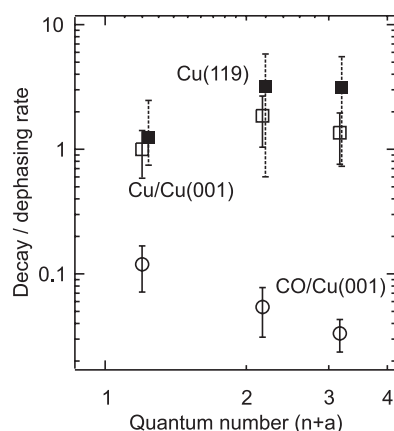
Figure 30. Ratio of the change of decay rate over the change of dephasing rate upon adsorption of Cu and CO on Cu(001) and for Cu(119) as a function of quantum number $(n + a)$ [26].

Since all scattering processes take place at the surface one naively expects that the branching ratio of inelastic and quasielastic scattering events is independent of n. While this roughly holds for Cu/Cu(001) it is obviously not fulfilled for CO/Cu(001) and Cu(119). For CO/Cu(001) the change of decay rate is $\propto (n + a)^{-3}$ while the change of dephasing rate decreases $\propto (n + a)^{-1}$ [10]. The difference of the branching ratios by more than one order of magnitude for the adsorbate systems is mainly due to the decay rate which is significantly larger for Cu than for CO on Cu(001) (see figure 25). In contrast the change of dephasing rate is similar for both adsorbate systems.

For the vicinal surfaces, dephasing of the $n = 1$ image-potential state is considerable while dephasing of higher-image-potential states ($n \geqslant 2$) is negligible. For the latter states interband scattering with large momentum transfer is dominant. Thus quasielastic scattering leads to immediate decay of the population rather than scattering of the electron within the image-potential state band itself (dephasing). For Cu on Cu(001) both processes have to be of comparable strength. This implies that large momentum transfer is more likely for a surface with steps as compared to a surface covered with individual adatoms. A reason may be that correlations in the step lattice invoke reciprocal lattice vectors which provide large momenta for quasielastic scattering processes.

Inelastic processes can be accounted for by an imaginary part of the potential, while the real part of the potential will determine elastic scattering rates. In a study of surface-state confinement in quantum corrals, Hörmandinger and Pendry have calculated transmission, reflection and absorption of electrons by chains of adatoms on an albeit flat surface [128]. For a repulsive potential they find strong absorption, whereas for an attractive scattering potential transmission and reflection, i.e., quasielastic scattering dominates. As mentioned, the different energy shift of the $n = 1$ image-potential state upon Cu and CO adsorption suggests a repulsive potential for Cu adatoms and an attractive potential for CO molecules and can at least qualitatively explain the different branching ratios of decay and dephasing observed.

A final comment of caution is advisable. As we have seen dynamics is strongly influenced by surface defects. Therefore absolute values of decay rates involve significant errors. In the present experiments decay rates on Cu(001) were typically 10% larger than in the experiments by Shumay *et al* [39], even though we used the very same sample and preparation recipes. It is likely that sample quality deteriorated during the course of the experiments. Electron

dynamics is an extremely sensitive probe of surface quality. It is even important to know how steps are oriented on the nominal flat surface. Note that it is not always true that the smallest decay rate corresponds to the best surface. Interband scattering caused by steps, i.e. defects, leads to refilling of the $n = 1$ image-potential-state band. Subsequent intraband decay will increase the population for $k_{\parallel} = 0$ and can seemingly lead to smaller intrinsic decay rates at the band bottom [36].

7. Concluding remarks

I hope I have convinced the reader that loosely bound electrons in image-potential states are a toy for femtosecond laser pulses. We can take part in the game by shaping the template on which electron dynamics takes place using well established surface science techniques.

The key to understand inelastic and quasielastic scattering processes turns out to be the momentum dependence of decay rates. On the stepped surfaces dynamics involves inter- and intraband-scattering processes which redistribute excited electrons from higher-to lower-image-potential states and within the image-potential-state band itself. On these surfaces interband-scattering processes are strongly asymmetric and attributed to irregularities in the step-induced superlattice. Steps are indeed a defect inherent to any surface in nature and I suppose that steps likewise cause interband scattering on the nominal flat Cu(001) surface. This lifts at least to some extent the discrepancy in decay rates found in experiment and calculated in many-body theory. We find a close resemblance of change of decay rate upon adsorption of CO with the decay rate on the flat Cu(001) surface. Data for Cu on Cu(001) show in contrast the trend observed for the stepped Cu(119) or Cu(117) surfaces. This suggests that for CO and Cu adsorbates different decay mechanisms are operative. I propose that for CO/Cu(001) decay is dominated by unoccupied adsorbate-induced resonances while for Cu/Cu(001) decay rates are in addition affected by interband-scattering processes.

It will be challenging to decorate steps with adsorbates and thereby modify the step potential. Using somewhat more complex molecules should allow us to introduce and study asymmetries in electron scattering. The extension to other materials will be a further necessary step towards an understanding of electron dynamics at metal surfaces. Image-potential states are certainly a curiosity, but an interesting one to study. Most of the concepts developed here can be applied to other electronic states, relevant for photochemical reactions and hot carriers in electronic devices.

References

[1] Dai H-L and Ho W (ed) 1995 *Laser Spectroscopy and Photochemistry on Metal Surfaces* (Singapore: World Scientific)
[2] Haight R 1995 *Surf. Sci. Rep.* **21** 275
[3] Petek H and Ogawa S 1997 *Prog. Surf. Sci.* **56** 239
[4] Hertel T, Knoesel E, Wolf M and Ertl G 1996 *Phys. Rev. Lett.* **76** 535
[5] Ge N-H, Wong C M, Lingle R L Jr, McNeill J D, Gaffney K J and Harris C B 1998 *Science* **279** 202
[6] Höfer U, Shumay I L, Reuß Ch, Thomann U, Wallauer W and Fauster Th 1997 *Science* **277** 1480
[7] Reuß Ch, Shumay I L, Thomann U, Kutschera M, Weinelt M, Fauster Th and Höfer U 1999 *Phys. Rev. Lett.* **82** 153
[8] Bonn M, Funk S, Hess C, Denzler D N, Stampfl C, Scheffler M, Wolf M and Ertl G 1999 *Science* **285** 1042
[9] Wolf M 1997 *Surf. Sci.* **377–379** 343
[10] Fauster Th, Reuß Ch, Shumay I L and Weinelt M 2000 *Chem. Phys.* **251** 111
[11] Echenique P M, Pitarke J M, Chulkov E V and Rubio A 2000 *Chem. Phys.* **251** 1
[12] Kentsch C, Kutschera M, Weinelt M, Fauster Th and Rohlfing M 2002 *Phys. Rev.* B **65** 075104
[13] Aeschlimann M, Bauer M, Pawlik S, Weber W, Burgermeister R, Oberli D and Siegmann H 1997 *Phys. Rev. Lett.* **79** 5158
[14] Knoesel E, Hotzel A and Wolf M 1998 *Phys. Rev.* B **57** 12812
[15] Campillo I, Rubio A, Pitarke J M, Goldmann A and Echenique P M 2000 *Phys. Rev. Lett.* **85** 3241
[16] Scholl A, Baumgarten L, Jacquemin R and Eberhardt W 1997 *Phys. Rev. Lett.* **79** 5146
[17] Hasselbrink E 1995 *Laser Spectroscopy and Photochemistry on Metal Surfaces* ed H-L Dai and W Ho (Singapore: World Scientific) ch 17, p 685
[18] Tom H W K and Prybyla J A 1995 *Laser Spectroscopy and Photochemistry on Metal Surfaces* ed H-L Dai and W Ho (Singapore: World Scientific) ch 20, p 827
[19] Petek H, Weida M J, Nagano H and Ogawa S 2000 *Science* **288** 1402
[20] Borisov A G, Gauyacq J P, Kazansky A K, Chulkov E V, Silkin V M and Echenique P M 2000 *Phys. Rev. Lett.* **86** 488
[21] Fauster Th and Steinmann W 1995 *Photonic Probes of Surfaces (Electromagnetic Waves: Recent Developments in Research)* vol 2, ed P Halevi (Amsterdam: North-Holland) p 347
[22] Steinmann W and Fauster Th 1995 *Laser Spectroscopy and Photochemistry on Metal Surfaces* ed H-L Dai and W Ho (Singapore: World Scientific) ch 5, p 184
[23] Kliewer J, Berndt R, Chulkov E V, Silkin V M, Echenique P M and Crampin S 2000 *Science* **288** 1399
[24] Chulkov E V, Sarria I, Silkin V M, Pitarke J M and Echenique P M 1998 *Phys. Rev. Lett.* **80** 4974
[25] Knoesel E, Hotzel A and Wolf M 1998 *J. Electron Spectrosc. Relat. Phenom.* **88–91** 577
[26] Weinelt M 2000 *Appl. Phys.* A **71** 493
[27] Echenique P M and Pendry J B 1978 *J. Phys. C: Solid State Phys.* **11** 2065
[28] Osgood R M Jr and Wang X Y 1997 *Solid State Physics* vol 51, ed H Ehrenreich and F Spaepen (San Diego, CA: Academic) p 1
[29] Plummer E W 1997 *Science* **277** 1447
[30] Hotzel A, Ishioka K, Knoesel E, Wolf M and Ertl G 1998 *Chem. Phys. Lett.* **285** 271
[31] Hotzel A, Knoesel E, Wolf M and Ertl G 1998 *Proc. SPIE* **3272** 228
[32] Berthold W, Höfer U, Feulner P and Menzel D 2000 *Chem. Phys.* **251** 123
[33] Berthold W 2001 *PhD Thesis* Technische Universität München
[34] Loudon R 1983 *The Quantum Theory of Light* (Oxford: Clarendon)
[35] Roth M, Pickel M, Wang J, Weinelt M and Fauster Th 2002 *Phys. Rev. Lett.* **88** 096802
[36] Berthold W, Güdde J, Feulner P and Höfer U 2001 *Appl. Phys.* B **73** 865
[37] Schäfer A, Shumay I L, Wiets M, Weinelt M and Fauster Th 2000 *Phys. Rev.* B **61** 13159
[38] Fischer R, Schuppler S, Fischer N, Fauster Th and Steinmann W 1993 *Phys. Rev. Lett.* **70** 654
[39] Shumay I L, Höfer U, Reuß Ch, Thomann U, Wallauer W and Fauster Th 1998 *Phys. Rev.* B **58** 13974
[40] Ogawa S, Nagano H, Petek H and Heberle A P 1997 *Phys. Rev. Lett.* **78** 1339
[41] Blum K 1983 *Density Matrix Theory and Applications* (New York: Plenum)
[42] Bloembergen N 1995 *Nonlinear Optics* (Singapore: World Scientific)
[43] Boger K, Roth M, Weinelt M, Fauster Th and Reinhard P-G 2002 *Phys. Rev.* B **65** 075104
[44] Dappe Y J, Villaeys A A and Lohner F P 2000 *Appl. Surf. Sci.* **41** 168
[45] Wolf M, Hotzel A, Knoesel E and Velic D 1999 *Phys. Rev.* B **59** 5926
[46] Ueba H and Mii T 2000 *Appl. Phys.* A **71** 537
[47] Weinelt M 2001 *Surf. Sci.* **482** 519

[48] Chebotayev V P 1976 *Springer Topics in Applied Physics* ed K Shimoda (Berlin: Springer) ch 6, p 201
[49] Hertel T, Knoesel E, Hotzel A, Wolf M and Ertl G 1997 *J. Vac. Sci. Technol.* A **15** 1503
[50] Wurth W, Rocker G, Feulner P, Scheuerer R, Zhu L and Menzel D 1993 *Phys. Rev.* B **47** 6697
[51] Karis O, Nilsson A, Weinelt M, Wiell T, Puglia C, Wassdahl N, Martensson N, Samant M and Stöhr J 1996 *Phys. Rev. Lett.* **76** 1380
[52] Wurth W 1997 *Appl. Phys.* A **65** 155
[53] Mårtensson N, Weinelt M, Karis O, Magnuson M, Wassdahl N, Nilsson A, Stöhr J and Samant M 1997 *Appl. Phys.* A **65** 159
[54] Keller C, Stichler M, Comelli G, Esch F, Lizzit S, Wurth W and Menzel D 1998 *Phys. Rev. Lett.* **80** 1774
[55] Wurth W and Menzel D 2000 *Chem. Phys.* **251** 141
[56] Kevan S D 1982 *Phys. Rev. Lett.* **50** 526
[57] Matzdorf R, Meister G and Goldmann A 1996 *Phys. Rev.* B **54** 14807
[58] Theilmann F, Matzdorf R, Meister G and Goldmann A 1997 *Phys. Rev.* B **56** 3632
[59] Nicolay G, Reinert F, Schmidt S, Ehm D, Steiner P and Hüfner S 2000 *Phys. Rev.* B **62** 1631
[60] Reinert F, Nicolay G, Schmidt S, Ehm D and Hüfner S 2001 *Phys. Rev.* B **63** 115415
[61] Höfer U, Shumay I L, Reuß Ch, Thomann U and Fauster Th 1998 *Proc. SPIE* **3272** 211
[62] Weida M J, Ogawa S, Nagano H and Petek H 2000 *Appl. Phys.* A **71** 553
[63] Weinelt M, Reuß Ch, Kutschera M, Thomann U, Shumay I L, Fauster Th, Höfer U, Theilmann F and Goldmann A 1999 *Appl. Phys.* B **68** 377
[64] Asaki M T, Huang C, Garvey D, Zhou J, Kapteyn H C and Murnane M M 1993 *Opt. Lett.* **18** 977
[65] Naganuma K, Mogi K and Yamada H 1998 *IEEE J. Quantum Electron.* **25** 1225
[66] Peatross J and Rundquist A 1998 *J. Opt. Soc. Am.* **15** 216
[67] Straub D and Himpsel F J 1984 *Phys. Rev. Lett.* **84** 1922
[68] Dose V, Altmann W, Goldmann A, Kolac U and Rogozik J 1984 *Phys. Rev. Lett.* **52** 1919
[69] Giesen K, Hage F, Himpsel F J, Rieß H J and Steinmann W 1985 *Phys. Rev. Lett.* **55** 300
[70] Schuppler S, Fischer N, Fauster Th and Steinmann W 1990 *Appl. Phys.* A **51** 322
[71] Schoenlein R W, Fujimoto J G, Eesley G L and Capehart T W 1988 *Phys. Rev. Lett.* **61** 2596
[72] Schoenlein R W, Fujimoto J G, Eesley G L and Capehart T W 1990 *Phys. Rev.* B **41** R5436
[73] Schoenlein R W, Fujimoto J G, Eesley G L and Capehart T W 1990 *Phys. Rev.* B **43** 4688
[74] Wolf M, Knoesel E and Hertel T 1996 *Phys. Rev.* B **54** R5295
[75] Echenique P M and Pendry J B 1990 *Prog. Surf. Sci.* **32** 111
[76] Harris C B, Ge N-H, Lingle R L Jr, McNeill J D and Wong C M 1997 *Annu. Rev. Phys. Chem.* **48** 711
[77] Smith N V 1985 *Phys. Rev.* B **32** 3549
[78] Goldmann A 1995 *Electronic Surface and Interface States on Metallic Systems* ed E Bertel and M Donath (Singapore: World Scientific) p 35
[79] Chulkov E V, Silkin V M and Echenique P M 1999 *Surf. Sci.* **437** 330
[80] Hulbert S L, Johnson P D, Weinert M and Garett R F 1986 *Phys. Rev.* B **33** 760
[81] Chulkov E V, Silkin V M and Echenique P M 1997 *Surf. Sci.* **391** L1217
[82] Sarria I, Osma J, Chulkov E V, Pitarke J M and Echenique P M 1999 *Phys. Rev.* B **60** 11795
[83] Giesen K, Hage F, Himpsel F J, Rieß H J, Steinmann W and Smith N V 1987 *Phys. Rev.* B **35** 975
[84] Goldmann A, Dose V and Borstel G 1985 *Phys. Rev.* B **32** 1971
[85] Giesen K, Hage F, Himpsel F J, Rieß H J and Steinmann W 1987 *Phys. Rev.* B **35** 971
[86] Kubiak G D 1988 *Surf. Sci.* **201** L475
[87] de Andres P L, Echenique P M and Flores F 1987 *Phys. Rev.* B **35** 4529
[88] de Andres P L, Echenique P M and Flores F 1989 *Phys. Rev.* B **39** 10356
[89] Pendry J B 1978 *Photoemission and the Electronic Properties of Surfaces* ed B Feuerbacher, B Fitton and R F Willis (Chichester: Wiley)
[90] Eberhardt W and Plummer E W 1980 *Phys. Rev.* B **21** 3245
[91] Levinson H J, Greuter F and Plummer E W 1983 *Phys. Rev.* B **27** 727
[92] Goldmann A, Altmann W and Dose V 1991 *Solid State Commun.* **79** 511
[93] Santoni A and Himpsel F J 1991 *Phys. Rev.* B **43** 1305
[94] Li D, Dowben P A, Ortega J E and Himpsel F J 1993 *Phys. Rev.* B **47** 12895
[95] Osma J, Sarria I, Chulkov E V, Pitarke J M and Echenique P M 1999 *Phys. Rev.* B **59** 10591
[96] McDougall B A, Balasubramanian T and Jensen E 1995 *Phys. Rev.* B **51** 13891
[97] Walter S, Baier H, Weinelt M, Heinz K and Fauster Th 2001 *Phys. Rev.* B **63** 155407
[98] Moritz W 2001 private communication
[99] Giesen M 1997 *Surf. Sci.* **370** 55
[100] Giesen M and Einstein T L 2000 *Surf. Sci.* **449** 191

[101] Frohn J, Giesen M, Poengsen M, Wolf J F and Ibach H 1991 *Phys. Rev. Lett.* **67** 3543
[102] Reinecke N, Reiter S, Vetter S and Taglauer E 2002 *Appl. Phys.* A **75** 1
[103] Poengsen M, Wolf J F, Frohn J, Giesen M and Ibach H 1992 *Surf. Sci.* **274** 430
[104] Braun J, Toennies J P and Witte G 1995 *Surf. Sci.* **340** 265
[105] Smoluchowski R 1941 *Phys. Rev.* **60** 661
[106] Besocke K, Krahl-Urban B and Wagner H 1977 *Surf. Sci.* **68** 39
[107] Wang X Y, Shen X J and Osgood R M Jr 1997 *Phys. Rev.* B **56** 7665
[108] Baumberger F 2001 private communication
[109] Krahl-Urban B, Niekisch E A and Wagner H 1977 *Surf. Sci.* **64** 52
[110] Ishida H and Liebsch A 1992 *Phys. Rev.* B **46** 7153
[111] Stumpf R and Scheffler M 1996 *Phys. Rev.* B **53** 4958
[112] Sánchez O, García J M, Segovia P, Alvarez J, de Parga A L V, Ortega J E, Prietsch M and Miranda R 1995
        Phys. Rev. B **52** 7894
[113] Fischer R, Fauster Th, von der Linden W and Dose V 1996 *Surf. Rev. Lett.* **3** 1393
[114] Baumberger F, Greber T and Osterwalder J 2001 *Phys. Rev.* B **64** 1954111
[115] Wang X Y, Shen X J, Osgood R M Jr, Haight R and Himpsel F J 1996 *Phys. Rev.* B **53** 15738
[116] Roth M, Pickel M, Wang J, Weinelt M and Fauster Th 2002 *Appl. Phys.* B **74** 661
[117] Davis L C, Everson M P, Jaklevic R C and Shen W 1991 *Phys. Rev.* B **43** 3821
[118] Ortega J E, Himpsel F J, Haight R and Peale D R 1994 *Phys. Rev.* B **49** 13859
[119] Berthold W, Höfer U, Feulner P, Chulkov E V, Silkin V M and Echenique P M 2002 *Phys. Rev. Lett.* **88** 056805
[120] Theilmann F, Matzdorf R and Goldmann A 1999 *Surf. Sci.* **420** 33
[121] DeMiguel J J, Sanchez A, Cebollada A, Gallego J M, Ferron J and Ferrer S 1987 *Surf. Sci.* **189/190** 1062
[122] Ernst H-J, Fabre F and Lapujoulade J 1992 *Surf. Sci.* **L275** 682
[123] Breeman M and Boerma D O 1992 *Surf. Sci.* **269/270** 224
[124] Dürr H, Wendelken J F and Zuo J-K 1995 *Surf. Sci.* **L328** 527
[125] Rogozik J, Dose V, Prince K C, Bradshaw A M, Bagus P S, Hermann K and Avouris P 1985 *Phys. Rev.* B **32**
        4296
[126] Tsuei K and Johnson P D 1992 *Phys. Rev.* B **45** 13827
[127] Egelhoff W F Jr and Jacob I 1989 *Phys. Rev. Lett.* **62** 921
[128] Hörmandinger G and Pendry J B 1994 *Phys. Rev.* B **50** 18607